

# **Investigation and Development of MR-Compatible Actuation Methods for Multi-Axis Robots**

**Xue Yin Zhang**

A thesis submitted in fulfilment  
of the requirements of the degree of  
Bachelor of Engineering (Mechatronic (Space))/Bachelor of Arts (Music)



Supervisor: André Kyme  
Co-supervisor: Graham Brooker  
School of Aerospace, Mechanical and Mechatronic Engineering  
The University of Sydney

November 2018



# Declaration

The work presented herein is substantially my own except for the contributions which is as follows:

- I conducted the literature survey that gives context to the work which has been carried out in this thesis project. At the start of this project, my supervisor provided me with a list of papers to guide my reading.
- I designed the model for the open loop ceramic motor jig with the help of Andrei Lozzi. The parts were then machined in the AMME workshop by Stanley Kakarda. I assembled the jig. I also wrote the program to control the motor with help from Brian Ki Myung Lee.
- André Kyme designed and constructed the closed loop ceramic motor jig from Lego with the (very helpful) assistance of his children.
- Full credit goes to Aidan McDaid from Boston University who designed, built, and tested the pneumatic rotary stepper motor during Semester 1 2018. McDaid also wrote the Arduino program to control the motor.
- I designed the CAD model for the pneumatic cylinder jig, fabricated its parts, and constructed the jig. I wrote the Arduino program to control the motor.
- I tested the above actuators at two MRI facilities with the help of Bin Dong, Sofie Trajanovska, Binh Pham, and Nana Sunn who operated the MRI scanners and conducted the scanning procedures. André Kyme assisted with the experimental setup and transport of equipment to and from our lab.
- I wrote the program to process the scan data on MATLAB with guidance from Bin Dong and Sofie Trajanovska on proper analytical procedure.

- I developed the pneumatic curvilinear stepper motor and designed the CAD models for it.
- I fabricated and constructed the acrylic curvilinear stepper motor prototypes.
- I fabricated and constructed the resin curvilinear stepper motor prototypes. Benjamin van Magill assisted with the first prototype, but fabrication of the subsequent prototype was carried out by myself.
- I wrote the Arduino program to control the pneumatic curvilinear stepper motor.
- I conducted experiments to measure load and bandwidth on the curvilinear motor, and was assisted by Graham Brooker and Mitch Bryson who provided advice on the testing procedure.

Signed:

**Xue Yin Zhang(student)**

Date:

**André Kyme (supervisor)**

Date:

**Graham Brooker (co-supervisor)**

Date:

# Abstract

Abstract text goes here...

If you've just opened up this template, you should check out Chapter 1 for a quick introduction. Note also that hyperlinks are rendered in colour for convenience during editing—see `../LaTeX/packages.tex`. Note also that there is a simple way to change all of the coloured hyperlinks to black in `../LaTeX/packages.tex`—look for `\usepackage[colorlinks`.

This paragraph is coloured in “highlightcolour”, defined in `../LaTeX/commands.tex`. To get rid of all highlighting in the document you can just redefine `highlightcolour`—see `\definecolor{highlightcolor}` in `../LaTeX/commands.tex`. Also have a look at `\definecolor{todo}` and `\definecolor{TODOcolour}` in the same file.



# Acknowledgements

I am indebted to a great many number of people who have each had a hand or a foot in pushing this thesis project forward. Deep gratitude and thanks go toward:

- **André Kyme** for sharing your intellect, knowledge, and spirit of dedication with me. Your unending support and guidance has been of immense help throughout the year.
- **Graham Brooker** for the indispensable advice you have offered along the way.
- **Gary Liney** for making this project possible.
- **Sofie Trajanovska, Binh Pham, Nana Sunn, and Bin Dong** for accommodating for our experiments with your time and resources.
- **Aidan McDaid** for your significant contribution to this project.
- **Andy Wan** for always being of assistance at the AMME Fabrication Lab whenever I asked for help.
- **Andrei Lozzi** for helping design the ceramic motor jig.
- **Ben van Magill** for teaching me how to use a resin printer.
- **Saree Analghy** for your expert advice and resources on motion-adaptive radiotherapy.
- **Brian Ki Myung Lee** for being a sounding board for all my ideas and challenges.
- **My immediate family** for your love and humour.

Why do scuba divers fall backwards off of the boat?

*Because if they fell forward, they'd still be in the boat.*

# Contents

<b>Declaration</b>	i
<b>Abstract</b>	iii
<b>Acknowledgements</b>	v
<b>Contents</b>	vii
<b>List of Figures</b>	ix
<b>List of Tables</b>	xi
<b>Acronyms</b>	xiii
<b>1 Introduction</b>	1
1.1 Background and motivations . . . . .	1
1.2 Project aim and scope . . . . .	3
1.3 Chapter structure . . . . .	4
<b>2 Literature Review</b>	5
2.1 Introduction . . . . .	5
2.2 MR-compatible materials . . . . .	6
2.3 Actuation, transmission, and control . . . . .	6
2.3.1 Ceramic motors . . . . .	7
2.3.2 Pneumatic actuation . . . . .	8

2.3.3	Hydraulics . . . . .	9
2.3.4	Mechanical transmission . . . . .	10
2.4	Applications of magnetic resonance (MR)-compatible robots . . . . .	10
2.4.1	Image-guided intervention . . . . .	10
2.4.2	Phantom manipulation and benchmarking of motion correction algorithms . . . . .	12
2.5	Summary . . . . .	13
<b>3</b>	<b>Methods</b>	<b>14</b>
3.1	Preliminary actuator design . . . . .	14
3.1.1	Ultrasonic motor design . . . . .	14
3.1.2	Pneumatic actuator design . . . . .	17
3.2	SNR Analysis . . . . .	25
3.2.1	Testing signal-to-noise ratio (SNR) on the 7T small animal system .	27
3.2.2	Testing SNR on the 1.5T MRI-LINAC . . . . .	30
3.3	Prototyping a pneumatic stepper motor . . . . .	33
3.3.1	Proof of concept . . . . .	35
3.3.2	Curvilinear stepper motor . . . . .	36
3.3.3	Circular track . . . . .	37
3.3.4	Fabrication . . . . .	38
3.3.5	Pneumatic control . . . . .	40
3.4	Actuator Characterisation . . . . .	41
3.4.1	Load tests . . . . .	43
3.4.2	Bandwidth tests . . . . .	45
<b>4</b>	<b>Results</b>	<b>47</b>
4.1	Preliminary actuator design . . . . .	47
4.1.1	Ceramic motor . . . . .	47
4.1.2	Pneumatic actuators . . . . .	47
4.2	SNR Analysis Results . . . . .	48

4.2.1	7T small animal system . . . . .	48
4.2.2	1.5T MRI-LINAC . . . . .	51
4.3	Pneumatic motor prototyping . . . . .	54
4.3.1	Proof of concept . . . . .	54
4.3.2	Acrylic prototypes . . . . .	55
4.4	Actuator Characterisation . . . . .	57
4.4.1	Load tests . . . . .	57
4.4.2	Bandwidth tests . . . . .	57
<b>5</b>	<b>Discussion</b>	<b>59</b>
5.1	Preliminary actuator design . . . . .	59
5.1.1	Ceramic motor . . . . .	59
5.1.2	Pneumatic actuators . . . . .	60
5.2	SNR Analysis . . . . .	61
5.2.1	The poor MR-compatibility of ceramic motors . . . . .	61
5.2.2	Choice of ROI . . . . .	61
5.3	Prototyping . . . . .	64
5.3.1	Air leakage . . . . .	64
5.3.2	Friction and tolerancing . . . . .	65
5.4	Actuator Characterisation . . . . .	65
5.4.1	Load tests . . . . .	65
5.4.2	Bandwidth tests . . . . .	66
<b>6</b>	<b>Conclusions</b>	<b>67</b>
6.1	Summary . . . . .	68
6.2	Future work . . . . .	68
<b>References</b>		<b>69</b>



# List of Figures

1.1	The 1.5T MRI-LINAC [1]	2
2.1	Ceramic motor with actuated parts labelled	7
3.1	Mechanical design for transmission of vibrating motor tip into rotary motion	15
3.2	Ceramic motor experimental setup - open loop	15
3.3	Closing the loop for a ceramic motor system	16
3.4	Ceramic motor dataflow diagram - close loop	16
3.5	Pneumatic system components	17
3.6	3D-printed rotary stepper motor. TODO: replace image with Aidan's Solid-works model instead	19
3.7	Switching the valves in the sequence 1-2-3-4 causes a clockwise rotation of the motor shaft	20
3.8	Pneumatic connections for the rotary stepper motor	20
3.9	Electrical connections for the rotary stepper motor	21
3.10	Deprag air motor	22
3.11	Pneumatic connections for the air motor	22
3.12	Electrical connections for the air motor	23
3.13	Double-acting cylinder	24
3.14	Pneumatic connections for the cylinder	24
3.15	States in the pneumatic cylinder system	25
3.16	Equipment setup during test scans	26
3.17	Phantom and scan slice setup	27

3.18 A ceramic motor is loaded at the edge of an RF coil, ready to be tested on the 7T scanner. Hidden from view is the falcon tube sitting in the middle of the RF coil. . . . .	28
3.19 Red = signal ROI, blue = background noise ROIs . . . . .	30
3.21 Stepper motors designed by Groenhuis et al (TODO: reference) . . . . .	34
3.23 A jig to demonstrate the stepping mechanism . . . . .	35
3.24 Three different iterations of design for a curvilinear stepper motor . . . . .	36
3.25 Circular track with sinusoidal teeth . . . . .	37
3.26 Example of all the distinct layers required for the prototype in Figure 3.24b (relative sizes are not to scale) . . . . .	39
3.27 Compressed flow air through the pneumatic system in its four possible states. Switching the valves in the sequence state 1-2-3-4 produce a counterclockwise movement of the motor relative to the circular track. Switching in the sequence state 4-3-2-1 produces a clockwise movement of the motor relative to the track. . . . .	40
3.28 Electrical connections for the four-chamber prototype actuator . . . . .	41
3.29 Bench-top setup for load and bandwidth tests. A bag is tethered to the end of the pulley system to hold the weights. . . . .	42
3.30 Close up of the pulley system . . . . .	43
4.1 SNR results from the 7T small animal system . . . . .	49
4.2 Sample original scan images from the 7T small animal system . . . . .	50
4.3 Sample scan images from the 7T small animal system with contrast adjusted to emphasise the image artefacts. . . . .	50
4.4 SNR results from the 1.5T MRI-LINAC (SE scans) . . . . .	51
4.5 Sample scan images from the 1.5T MRI-LINAC (SE scans) . . . . .	52
4.6 Sample scan images from the 1.5T MRI-LINAC with contrast adjusted to emphasise the image artefacts (SE scans) . . . . .	52
4.7 SNR results from the 1.5T MRI-LINAC (HASTE scans) . . . . .	53
4.8 Proof of concept for stepping mechanism . . . . .	54
4.9 Pressurising chambers in the order 1-2-3-4 causes track to move to the right	55
4.10 Acrylic prototypes – four chamber, curvilinear track design . . . . .	55
4.11 Resin prototypes – curvilinear track design . . . . .	56

4.12 Experimental results for load capacity . . . . .	57
4.13 Experimental results for bandwidth capacity . . . . .	58
5.1 Contrast-adjusted scan image with ROI overlaid (7T small animal system) (red = signal ROI, blue = background ROI). Background ROI misses the ringing artefacts (left) but overlaps with the radiofrequency (RF) noise artefacts (right) . . . . .	62
5.2 Vertical background ROIs for 7T small animal system data . . . . .	62
5.3 Hypothetical SNR analysis results for vertical background ROIs for the 7T small animal system data . . . . .	63
5.4 Most air leakage occurred at the sides of the acrylic curvilinear stepper motor	64
6.1 6-DOF Stewart platform with curvilinear stepper motors as carriages on a circular track . . . . .	68



# List of Tables

1.1	Desired specifications . . . . .	4
3.1	Pneumatic system components . . . . .	17
3.2	Bill of equipment . . . . .	18
3.3	Test configurations on the 7T small animal system . . . . .	28
3.4	MRI scan parameters for our first test on the 7T small animal system . . .	29
3.5	MRI scan parameters for test one on the 1.5T MRI-LINAC . . . . .	31
3.6	MRI scan parameters for test two on the 1.5T MRI-LINAC . . . . .	31
3.7	Test configurations on the 1.5T MRI-LINAC . . . . .	32
3.8	Values for the standing wave parameters in the sinusoidal circular track. .	38
3.9	Activated outlet ports in each valve for each system state . . . . .	41
3.10	Known masses in the pulley system . . . . .	43
3.11	Experimental parameters for the load tests . . . . .	45
3.12	Experimental parameters for the bandwidth tests . . . . .	46



# **Acronyms**

<b>CAD</b>	computer-aided design
<b>DOF</b>	degree-of-freedom
<b>HASTE</b>	half-Fourier acquisition single-shot turbo spin-echo
<b>fMRI</b>	functional magnetic resonance imaging (MRI)
<b>FOV</b>	field of view
<b>ID</b>	inner-diameter
<b>IGI</b>	image-guided intervention
<b>LINAC</b>	linear accelerator
<b>MR</b>	magnetic resonance
<b>MRI</b>	magnetic resonance imaging
<b>OD</b>	outer diameter
<b>RF</b>	radiofrequency
<b>ROI</b>	region of interest
<b>SE</b>	spin echo
<b>SNR</b>	signal-to-noise ratio



# Chapter 1

## Introduction

### 1.1 Background and motivations

When someone is diagnosed with cancer, one of the treatments that may be offered to the patient is radiotherapy. What radiotherapy does is it delivers a radiation beam at cancerous cells while sparing the surrounding normal tissue, but the efficacy of such a treatment is often hampered by natural physiological movements which cause tumours to deviate from the radiation beam centre. One way to deal with the problem of natural physiological movements is to employ a technique called motion-adaptive radiotherapy. In motion-adaptive radiotherapy, the patient is imaged at the same time as the radiotherapy treatment. The idea is that the motion-adaptive system can use the knowledge of a patient's real-time movements to compensate for the motion of a target tumour during the delivery of the radiation dose.

Currently in Australia, there is a motion-adaptive radiotherapy system being developed that has gained a lot of research interest in the past few years. This system is called the MRI-LINAC, one of just seven known systems in the world, which is the combination of an MRI scanner to provide the medical imaging and a linear accelerator (LINAC) to deliver the radiation treatment through a split in the bore of the MRI scanner. The challenge with

the MRI-LINAC system is that there is – at present – no standard procedure for testing the performance of the system. Without quality assurance testing of the MRI-LINAC, there is no way of knowing whether the system is able to deliver radiotherapy treatment that is truly motion-adaptive. This is the problem gap that this thesis aims to address: we need a way of producing known, reproducible movements within the MRI-LINAC for quality assurance testing of the motion-adaptive radiotherapy system. Put another way, we need a robotic system that can be placed inside the MRI-LINAC to simulate natural physiological movements as a source of ground truth for quality assurance testing of the MR-guided radiotherapy system.

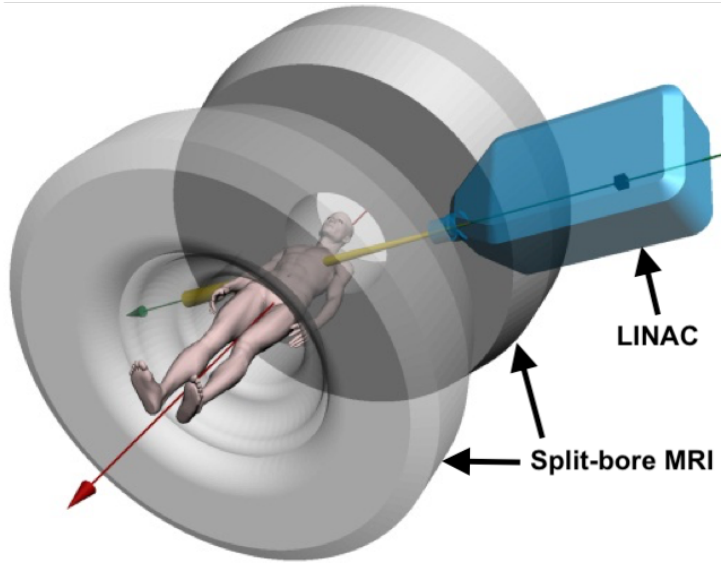


Figure 1.1: The 1.5T MRI-LINAC [1]

MRI scanners, however, are a notoriously difficult environment to operate within because of its extremely high magnetic field strength and switching magnetic field gradient during the scanning process. Any object made from ferromagnetic materials will be attracted to the scanner and become a projectile hazard and cause a lot of damage the patient and the if the object is untethered. Moreover, conventional electronic sensors and motors will behave unexpectedly under such a strong magnetic field as an MRI scanner. Making a robotic system fully MR-compatible is no trivial matter considering the sophistication of

conventional electronics that can no longer be used anymore within an MR environment. In addition to the very high magnetic field strength, there is also the added complexity of accessibility to the machine. Space is already limited inside the bore of an MRI scanner with a patient in it, let alone room for a robotic system, and if the robotic system relies on ferromagnetic devices to operate, these ferromagnetic devices will have to be taken outside of the scan room, therefore necessitating long cables between the control devices outside the scan room and the robotic system inside.

As difficult as this sounds, the pay-off for using MRI technology is that it offers excellent soft tissue contrast without the ionising radiation exposure that imaging modalities like PET, CT, and X-ray rely on to produce its scan images. By overcoming the hurdle of operating mechatronic systems within the harshness of an MR environment, novel MR-guided radiotherapy systems like the MRI-LINAC have the potential to become a superior, minimally-invasive, form of treatment for cancer patients.

## 1.2 Project aim and scope

The aim of this thesis project is to develop actuators that can be scaled into a multi-axis robotic platform for the purpose of quality assurance of MR-guided radiotherapy. What this entails is the:

- Investigation of MR-compatible actuation methods, with a particular focus on ultrasonic motors and pneumatic actuators as potential candidates for suitable actuators
- Design, fabrication, testing, and characterisation of prototype actuators
- Design of a prototype robotic platform for possible future development

To guide the design process of prototype actuators, there are number of criteria would be desirable in a future robotic platform:

---

Criteria	Value
Payload	1kg
Range of motion	$\pm 20^\circ$ rotations
Trajectory sampling rate	3.3 Hz

---

Table 1.1: Desired specifications

The payload criteria is related to the weight of an imaging phantom that the robotic platform would have to able to support when performing quality assurance testing. The other criteria are related to the most extreme physiological movements that the platform is expected to simulate: lung expansion and contraction [2].

## 1.3 Chapter structure

This thesis is structured as follows:

**Chapter 2** is a literature review of the current research landscape of MR-compatible robotic systems. There is a discussion of key past developments which influence and give context to the work that has been carried out in this thesis project.

**Chapter 3** explains the methods that were used to design, build, and test a number of prototype MR-compatible actuators.

**Chapter 4** lists the results that characterise our MR-compatible actuator over a number of key metrics for successful actuator design.

**Chapter 5** contains a discussion and an in-depth analysis of the experimental results. It offers an interpretation of the data, and what it means for the viability of the MR-compatible actuator developed.

**Chapter 6** summarises the main developments to come out of this thesis project, and also suggests possible future work to extend what has been currently been achieved.

# Chapter 2

## Literature Review

### 2.1 Introduction

As an imaging modality, MRI technology has proven itself to be a highly advanced diagnostic tool that has been in widespread clinical use for a long time already. As mentioned earlier in the introduction, MRI technology has the benefit of producing high quality images without the ionising radiation exposure of other modalities like CT scans and X-ray imaging. Even when compared to ultrasound imaging, which does not use ionising radiation, MRI offers a higher contrast visualisation of soft tissues in both the target and surrounding area [3], making MRI a desirable instrument for precision applications.

Regarding the operating principles of an MRI scanner, the scanners use a very strong magnetic field – usually between 0.5-7T – to align the spin axes of the hydrogen protons in the subject's body into a unidirectional magnetic vector [4]. The scanner then emits a high frequency RF pulse which causes the magnetic vector of hydrogen to relax, emit energy, and generate a signal which can be detected to form an MRI scan image [4]. By changing the gradient of the magnetic field, different slices of the body may be imaged. In short, MR-compatible components must be able to tolerate three hostile conditions:

(1) very strong magnetic fields, (2) high frequency RF pulses, and (3) switching magnetic field gradients [5].

## 2.2 MR-compatible materials

For a piece of equipment to be considered MR-compatible, it must be made from non-ferromagnetic materials. If one was not careful and introduced a ferromagnetic component into the scanner, it could become a hazardous projectile due to the interaction between the magnetic field of the scanner and the ferromagnetic component. Not only must materials be non-ferromagnetic, but they should also be non-conductive, as the switching magnetic gradient of the scanner could induce eddy currents within the component and cause artefacts in the scan image [5]. That said, conductive and non-ferromagnetic parts are permissible as long as they are small and secured down [3].

Ideal materials for best MR-compatibility are plastics, ceramics, and composites. Non-ferromagnetic metals like titanium, and zinc are also acceptable – and commonly used too – because the dangers of generating eddy currents is low. The non-ferromagnetic metals that offer higher MR-compatibility are beryllium copper (CuBe), phosphorous copper (CuP), and brass [6]. When choosing materials for MR-compatible design, there is a trade-off between the stiffness and strength of metal, and the passivity plastics and ceramics.

## 2.3 Actuation, transmission, and control

Moving on to the meat of the matter, the real challenge in MR-compatible robotics is in the limited range of actuations methods available to work with. In a 2006 review of MR-compatible actuators, Gassert et al. [5] determined that suitable actuation methods for MR environments include pneumatics, hydraulics, electroactive polymers, cable/rod

transmission, ultrasonic motors, and magnetomechanics, as these methods of actuation have evidence and precedence of success in the academic literature.

### 2.3.1 Ceramic motors

A ceramic motor<sup>1</sup> uses the vibration of its motor tip to drive whatever is loaded on the motor tip. The way the motor works is that a motor driver applies a high frequency, high voltage, and low current signal across a piece of ceramic, which then induces an ultrasonic vibration in the ceramic motor tip under the piezoelectric effect [3]. When the motor tip is coupled with a ceramic strip and linear slide, the vibrations will translate into linear motion of the strip. On the other hand, if the motor is coupled with a ceramic ring and bearing, the vibrations will translate into rotary motion.

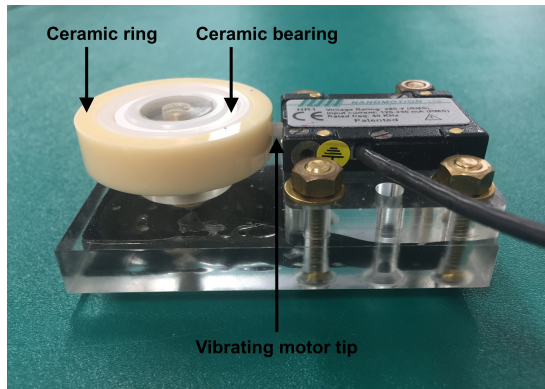


Figure 2.1: Ceramic motor with actuated parts labelled

Benefits of a ceramic motor include their compact size, nanoscale precision control, high bandwidth of at least 50Hz [5], and non-backdrivability. Although non-backdrivability would actually be a detriment to some robotic applications where human interaction is desired, it would actually be advantageous in our application as a MR-guided radiotherapy benchmarking tool where a robotic manipulator has to consistently drive a heavy payload.

There are, however, many drawbacks to ceramic motors. The biggest flaw reported by research is the moderate-to-severe drop in image SNR when the motor is in motion at the

---

<sup>1</sup>Ceramic motors are also interchangeably called piezoelectric motors or ultrasonic motors

same time as the MRI scanning process [7–10]. To mitigate this problem, some ceramic motor robotic systems were designed to be placed further away from the isocentre of the scanner [11], with others even requiring extra transmission to deliver actuation from outside the scanner into the destination within the scanner [12].

Many of the earliest seminal works in the field of MR-compatible robotics have used ceramic motors as their principle actuation method in their robotic designs [12–14]. In more recent developments, researchers have devised robotics systems where they switch off the ceramic motors during scanning [3, 10], but that's not feasible for our application where the robotic system is meant to be moving during the scan.

This is the reason why we are interested in investigating ceramic motors. They have qualities that are very desirable – compact and precise – but also have undesirable qualities – poor SNR performance – that demand further investigation.

### 2.3.2 Pneumatic actuation

Many literature reviews agree that pneumatic tubes are best option for maintaining a high SNR [3, 5, 7]. In addition to high SNR performance, pneumatically actuated systems are easily transportable to an MRI scanner room as hospitals would normally have pneumatic compressors readily available, and do not require a return path for the air or for any leakage of air [5]. On the downside, pneumatic actuation has a relatively low bandwidth, reaching up to 10Hz bandwidth for shorter tube transmission, and a time delay between the compressor and the actuator due to the compressibility of air [3]. The compressibility of air also causes low stiffness in the robotic joints, making it suitable only for smaller loads.

Traditionally, pneumatics have also been difficult to apply continuous servo-control of a pneumatic joint because of various characteristics of air such as [15, 16]:

- Slow travel and response time, especially in long pneumatic lines (low bandwidth)

- Non-linearities in pneumatic lines and actuators due to the compressibility of air  
(complicated control problem to solve)

2007 proved to be a formative year for pneumatic motors after Stoianovici et al. [16] published their work on a pneumatic stepper motor called ‘PneuStep’, using a simple guiding principle: pneumatic pistons can be modelled as a binary actuator by only considering the two end states of said piston. By coupling together multiple pistons for the actuation of one joint, pneumatic motors were able to be controlled in discrete steps rather than as a continuous actuator as was previously the norm.

In this “new step” towards an inclination for stepper motor design, research interest very quickly began to shift to pneumatic design and how it might be further improved. The academic conversation also progressed from how one might linearise the control of pneumatic servo motor [15], to how might a pneumatic stepper motor be coupled to produce better resolution than Stoianovici et al. had achieved [17–20] right down into the tens of microns level of position control precision [20]. At the same time, much of the rapid development of prostate procedures post-2007 also began with Patriciu et al. being early adopters of the PneuStep motor [21]. Pneumatic stepper motors also have excellent SNR losses both when stationary as well as in motion [7].

As well as ceramic motors, pneumatic stepper motors are of interest to this project due to desirable traits like adequate open-loop performance and superior SNR performance.

### 2.3.3 Hydraulics

Although it may appear that pneumatics are a strong front-runner for MR-compatible actuation due to the sheer research attention devoted to them, hydraulics are still being developed, tested and validated; at this year’s International Conference on Robotics and Automation (ICRA), a hydraulically actuated MR-compatible robot won a best paper award [22].

Hydraulics have the advantage of high hose flexibility, and does not have problems associated with compressibility, with up to 20Hz bandwidth for shorter transmission lengths [5]. However, hydraulic systems can also be problematic due to high joint friction [5] and the safety hazards of fluid leakage or the introduction of air bubbles in the pressure system [3]. Hydraulics were ruled out for this project due to the dangers of improper hydraulics maintenance and the need for specialised knowledge and training in the area.

### **2.3.4 Mechanical transmission**

Cables, shafts, and rods have been used successfully in the past [3, 5], but the need for fixed infrastructure make mechanical transmission too cumbersome and impractical for a clinical MRI setting. Tele-operated robotic systems [23, 24] are also unsuitable for our purposes as they do not meet the reproducibility criteria.

## **2.4 Applications of MR-compatible robots**

Recent advancements in MRI technology and increasing research interest in the imaging modality has created a demand for the use of robotic systems inside the MRI scanner. In the current state of the art, researchers have been developing robotic systems for highly specialised applications in image-guided intervention (IGI) and rehabilitation rehabilitation therapy during functional MRI (fMRI).

### **2.4.1 Image-guided intervention**

IGI is by far the the most well-reported application of MR-compatible robotics. There is a wide body of literature on the niche field of IGI MR-compatible robotics from which we draw influence and seek inspiration for this thesis project.

Recent work in pneumatic stepper motors have contributed to successes in MR-guided stereotactic surgeries, especially in prostate biopsy and brachytherapy.

Stereotactic surgery is by far the most well-reported application of MRI-guided intervention in the academic literature. Ever since Masamune et al's [14] pioneering work on an 6-DOF MR-compatible needle insertion manipulator in 1995 – arguably quite a few years ahead of their time – robotics researchers began to grow an interest in MR-guided breast biopsy [23, 25], and stereotactic neurosurgery [22].

Especially in the last ten years, the overwhelming majority of developments, however, are concerned with prostate procedures, which has gained a lot of traction [21, 26–31]. Of the various prostate surgeries available, the most common two are: (1) biopsy, for diagnosis of prostate cancer, and (2) brachytherapy, the delivery of radioactive seeds right at the site of the tumours, so as to minimise unnecessary radiation exposure on healthy tissue.

Part of the growth in academic interest in MR-guided prostate exams is that the current standard – then and now – for prostate biopsy is at best a random sampling of biopsy cores under the guidance of transrectal ultrasound, which has poor tumour localisation sensitivity [26]. In 1999, Chinzei et al had laid the groundwork for appropriate design criteria of MR-compatible mechatronic devices [6] and then later also published an example of a 5-DOF ultrasound-actuated manipulator that built upon the findings of Masamune et al's earlier work. Another reason why prostate procedures, specifically, grew in popularity is that typical MRI bores are around 60cm in diameter [23] – so space is limited – and the best place to fit a sizeable robot is between the legs of the patient straddling the robot [26, 27], or, alternatively with the patient lying on their side with their hips and knees at 90° as if sitting on the robot [28]. This way, the robot is not does not intersect with the imaging slice except for the needle tip during insertion, thus allowing for greater flexibility in choice of materials that might cause SNR losses but are more rigid.

With needle insertion applications, the highest priority for performance is position accuracy of the end effector, which is typically a sheath or tube with a needle inside. Even with Masanume et al's [14] early needle insertion manipulator, the team was able to achieve at

worst 3mm accuracy with image feedback from an MRI scanner, which at the time had 1mm resolution and was part of the reason why the upper error bound was as large as 3mm. Recent works easily achieve sub-millimetre position accuracy [20].

Accurate as they may be, robotic systems designed for needle insertion and stereotactic purposes have design features that would not be appropriate for a fast and reproducible robotic system for phantom manipulation. One feature would be that needle insertion robots are built with an end effector that provides translational motion for the needle to extend and retract, whereas either a gripper or a simply platform would be a more reasonable robot interface for a phantom manipulator. Another feature is the fixing of parts and joint configuration: a platform such as a pan-tilt would require two fixed points for each axis of rotation, rather than the one sided fixture of needle insertion devices.

General-purpose robotic systems for IGI have been reported before [13, 31, 32], though they tend to be few and far between, and most other robotic systems target a particular task like prostate biopsy or brachytherapy. The general-purpose robotic system can take the form of a multi-degree-of-freedom (DOF) robot arm that can be tele-operated [31, 32] or the form of a 6-DOF platform that resembles a CNC mill. Both these types of designs would be inappropriate for our purposes as they have been designed with the intent of having a medical instrument as the end effector. In a robotic arm system, driving a 1kg phantom payload would apply a high torque load on each individual joint in the arm, whilst in a mill-like system, the would TODO: FINISH SENTENCE

## 2.4.2 Phantom manipulation and benchmarking of motion correction algorithms

During the time that an MRI scanner takes to capture an image, the patient may have moved a little – as is natural for living and breathing things – and produce artifacts in the image that must be corrected for, which is in itself its own challenge. At the moment, there is no consensus of single best motion correction algorithm, nor of a benchmarking

technique to compare the results of an algorithm to.

Without going into details about different motion correction algorithms, previous and current benchmarking tools in use are a mixed bag of qualitative assessment of image quality, and quantitative techniques, including: offline computer simulations [33], use of fiducial markers [34], checkerboard calibration [35], and manual movement of reference phantoms [35]. The same problem exists from functional MRI where there is a lack of a noiseless ground truth with which to compare the results of motion correction techniques [36].

As mentioned in Chapter 1, the goal is prototype a phantom manipulator that can act as a benchmarking tool for motion correction algorithms by actuating known movements and speeds as a source of an accurate and robust the ground truth. Although this application of an MR-compatible robot is very different from the common research interest of MR-guided medical intervention, there is still a plethora of robotics development that would be hugely informative for this project.

## 2.5 Summary

All things considered, the phantom manipulator application of MR-compatible robotics that we are pursuing leaves a lot of room for discovery, as current research interest is focussed on IGI. That said, the rapid development of ceramic motor systems and the pneumatic stepper motor in IGI application show promise and demand further investigation of viability.

# Chapter 3

## Methods

### 3.1 Preliminary actuator design

The first step in this project was to develop a series of actuators in order to understand the range of MR-compatible actuation methods available at our disposal. By testing and comparing the different types of actuators, we can make an assessment of their viability in a larger scale, multi-DOF robotic system with regard to the actuator's practicality and its SNR performance in an MRI environment.

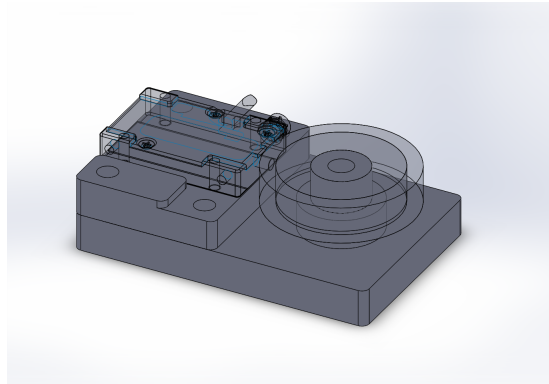
Specifically, we have tested an ultrasonic motor and three other actuators driven by pneumatics: a rotary stepper motor, air motor, and cylinder. The design and development of each actuator is detailed in this section.

#### 3.1.1 Ultrasonic motor design

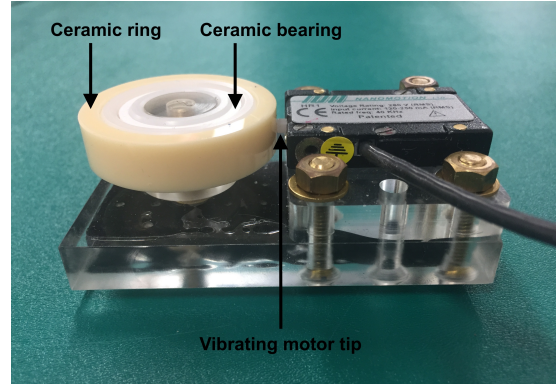
This section details the design of the Nanomotion HR1 motor. The Nanomotion HR1 motor is not your typical motor in that you cannot plug-and-go straight out of the box. It requires a number of supporting hardware to control and drive the motor, and has strict mechanical pre-loading requirements before the motor can be operated.

## Mechanical design

TODO: short explanation of jig



(a) Design model



(b) Built model

Figure 3.1: Mechanical design for transmission of vibrating motor tip into rotary motion

## Hardware architecture

In an open loop system, the control chain begins with the Galil Motion Controller TODO: explanation of devices

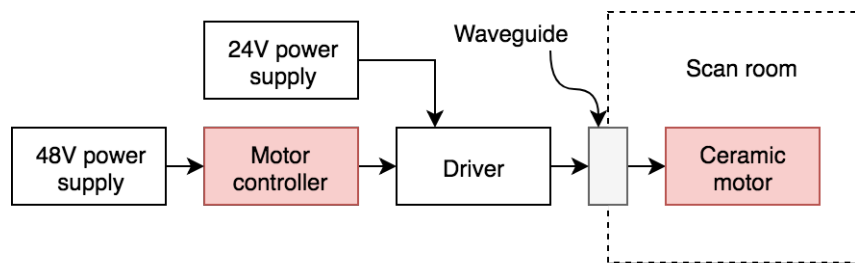


Figure 3.2: Ceramic motor experimental setup - open loop

### Closing the loop

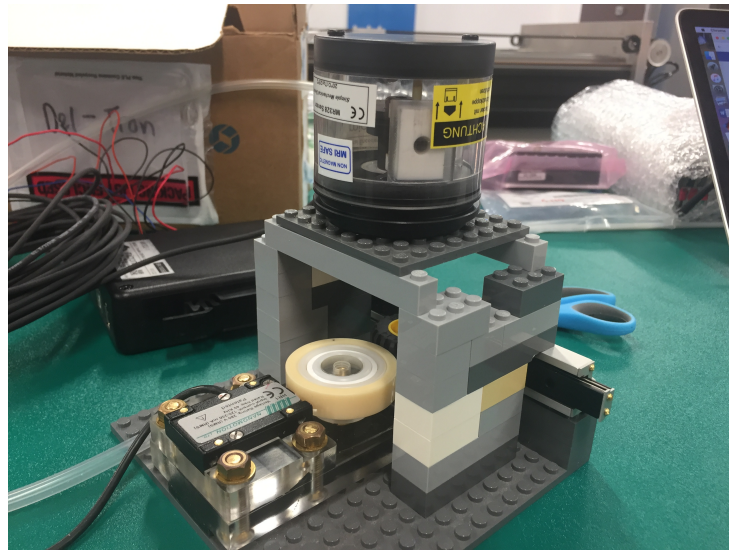


Figure 3.3: Closing the loop for a ceramic motor system

In a closed loop system, a ceramic bearing is coupled with a small rubber wheel. The rubber wheel drives the linear slide, which provides the compressive force to couple the wheel to the ceramic bearing. An MR-compatible optical encoder is then coupled to the rubber wheel via a rubber tube – not visible in picture – which lessens the load on the coupling shaft of the encoder.

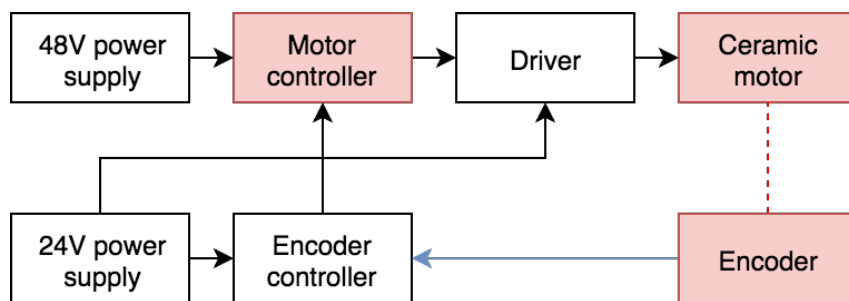


Figure 3.4: Ceramic motor dataflow diagram - close loop

### 3.1.2 Pneumatic actuator design

The second actuation method we have tested is pneumatics. Unlike the ceramic motor, pneumatically driven actuators can have a number of different principles of actuation, a few of which have been tested by us. Diverse as they are, most pneumatic actuation systems require the same basic components:



(a) Compressor

(b) Valves

(c) Controller

(d) Pneumatic tubes

Figure 3.5: Pneumatic system components

Component	Purpose
Compressor	Stores and supplies compressed air to the rest of the system
Valves	Directs compressed air from the inlet into the desired outlet
Controller	Controls and switches the valves
Pneumatic tubes	Transport compressed air to the actuator

Table 3.1: Pneumatic system components

Model	Details
Chicago HUSH 50 Air Compressor	Fitted with a water filter and line pressure gauge
Mindman 5/2 Valves	Five port, two state valve with: <ul style="list-style-type: none"> <li>• 1 inlet port</li> <li>• 2 outlet ports</li> <li>• 2 exhaust ports</li> </ul>
Arduino Due	Mounted with an Arduino 4 Relays Shield
Pneumatic tubes	Two sizes used: <ul style="list-style-type: none"> <li>• 5mm inner-diameter (ID), 8mm outer diameter (OD)</li> <li>• 4mm ID, 8mm OD</li> </ul>

Table 3.2: Bill of equipment

Some pneumatic actuators have a continuous range of motion and require continuous control over air pressure to produce varying speeds. Other actuators have a discrete range of motion and rely on a fixed air pressure and switching valves to produce stepped motion. Different actuators require us to connect these components up into different configurations.

### Rotary stepper motor

This rotary stepper motor is modelled after the Bourke engine, which was first - Groenhuis

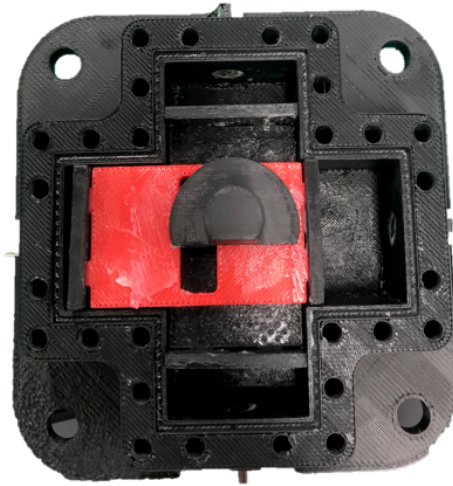


Figure 3.6: 3D-printed rotary stepper motor. TODO: replace image with Aidan's Solid-works model instead

This motor has four inlet ports, each of which lead into a chamber with a piston inside it.

With four pistons and chambers, the stepper motor has capable of producing 90 degrees (insert degrees symbol!) of motion for each step.

Also known as a Bourke engine. Designed by Aidan McDaid, an exchange student from Boston University who worked on this project in Semester 1 2018. The motor is mostly composed of 3D-printed PLA (put in acronym????????) parts, as well as rubber sheets and silicone to create a seal in the chamber, and nylon screws to hold the 3D-printed parts together.

INSERT TABLE OF BASIC SPECS THAT AIDAN WAS ABLE TO QUANTIFY

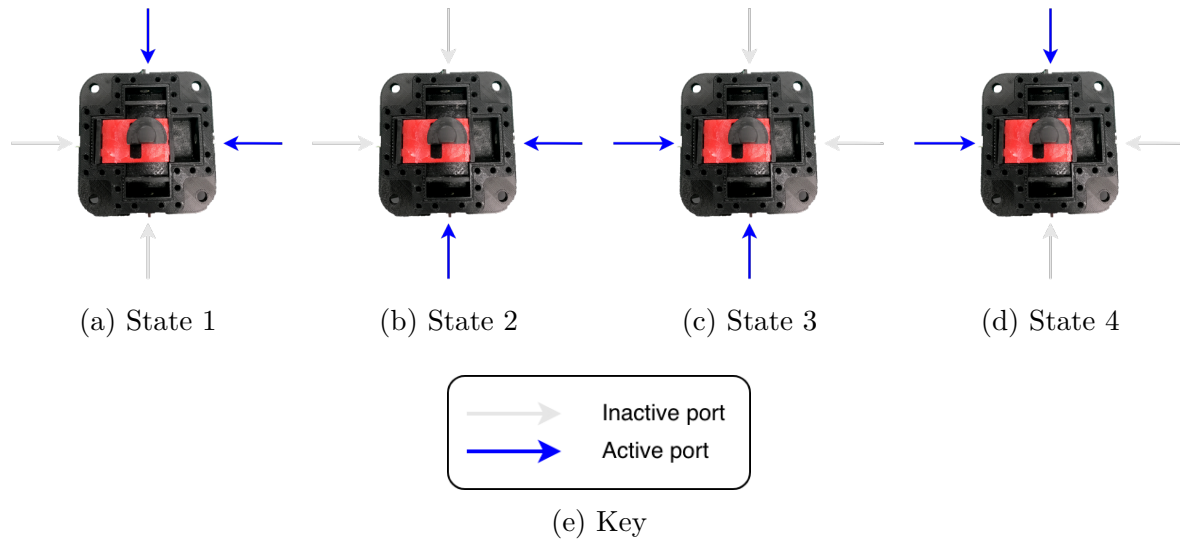


Figure 3.7: Switching the valves in the sequence 1-2-3-4 causes a clockwise rotation of the motor shaft

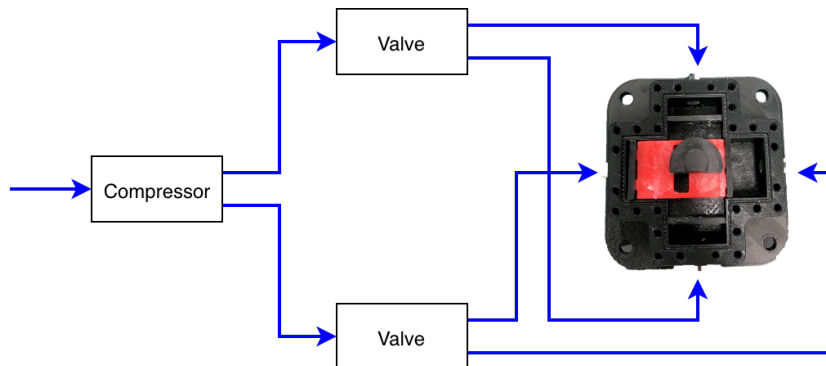


Figure 3.8: Pneumatic connections for the rotary stepper motor

As shown in Figure 3.8, pressurised air flows from the compressor into the two valves, which then directs the air into an outlet depending on the control signal from the Arduino. Each valve can only have one of its two outlets active at a time and must have its outlets on opposite sides of the stepper motor. There are no outlet ports on the motor to exhaust compressed air. Instead, air is exhausted through the cracks and crevices where the motor does not have an airtight seal, especially because the 3D-printed parts are slightly porous.

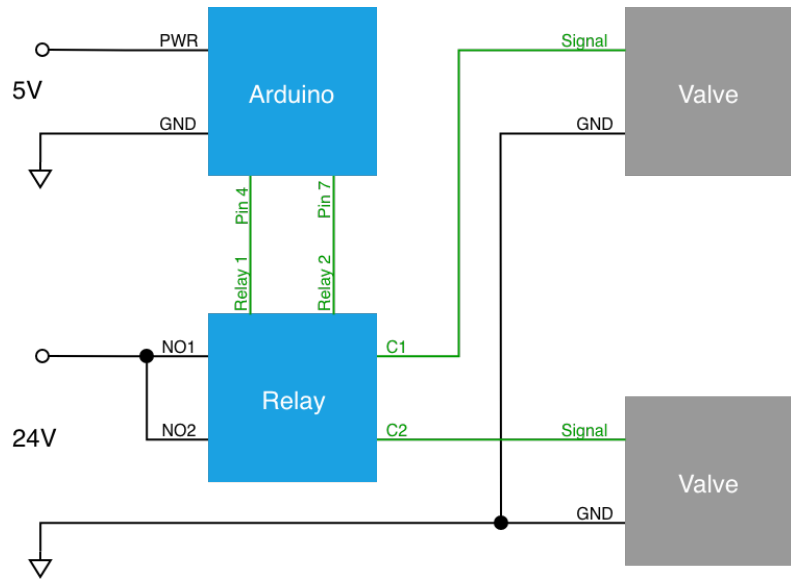


Figure 3.9: Electrical connections for the rotary stepper motor

Because the valves require a higher voltage and current output than can be supplied by the Arduino Due, we have used an additional 24V power supply and relay (the Arduino 4 Relays Shield) to deliver power to the valves. These components are wired as shown in Figure 3.9

### Air motor

Air motors resemble DC motors in that both have a rotating shaft that can produce continuous motion over a range of speeds. The air motor we have is custom-made with non-ferromagnetic parts from the German manufacturer Deprag. The motor has two air inlets – one for each direction of rotation, clockwise and counterclockwise – and one air outlet to exhaust the compressed air. Increasing the pressure to either of the inlet ports increases the speed of shaft rotation.

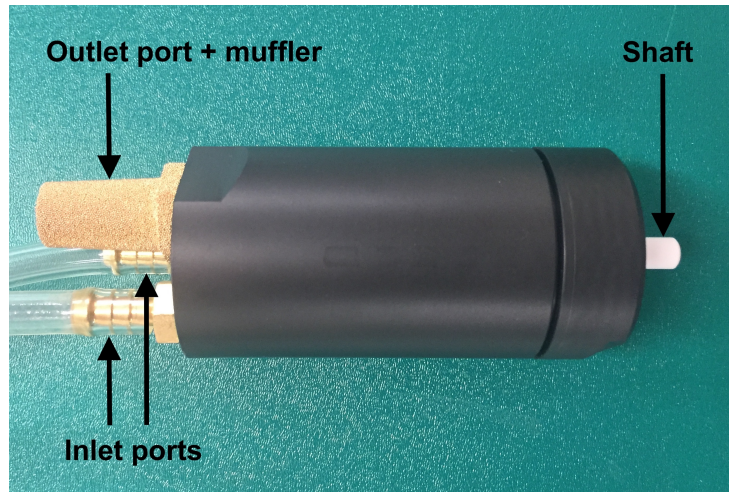


Figure 3.10: Deprag air motor

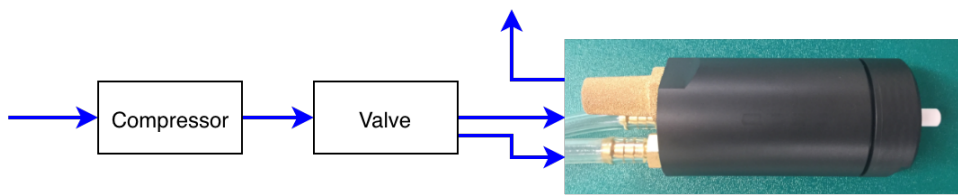


Figure 3.11: Pneumatic connections for the air motor

Because we don't have a pneumatic pressure controller, the design for this air motor is limited to just one valve which switches the direction of motion. With a fixed air pressure determined by the pressure gauge on the compressor, the motor operates at a fixed speed in both directions of rotation. This leads to a very simple electrical setup (Figure 3.12):

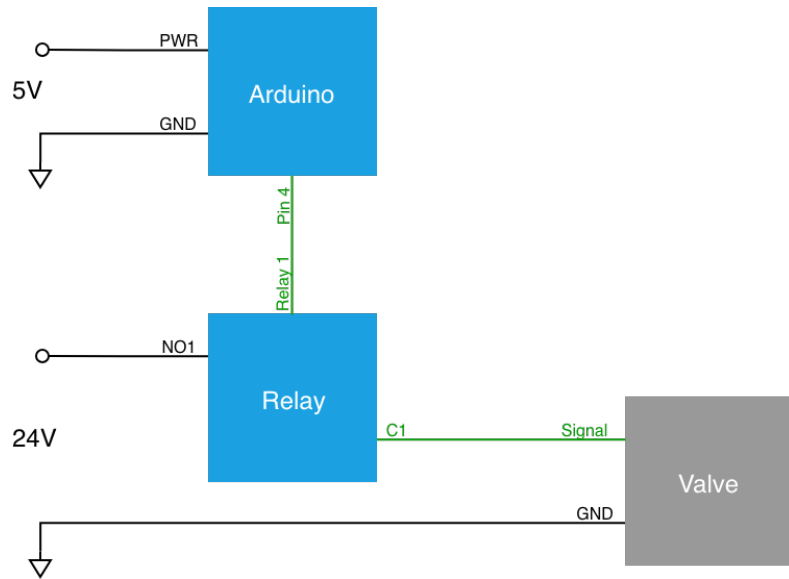


Figure 3.12: Electrical connections for the air motor

### Double-acting cylinder

In a pneumatic cylinder, the compressed air causes a piston to extend and retract linearly. This is different from the previous two pneumatic motors which use compressed air to produce rotary motion. A double-acting cylinder has two ports, where when one port becomes pressurised, the other port must act as an exhaust, and vice versa.

Pneumatic cylinders are very simple to set up, except that for our cylinder, the piston should never be allowed to reach its maximum extension or retraction. This is because our MR-compatible cylinder is made from glass<sup>1</sup>, and the force of the compressed air can cause the pistons to damage the stoppers at either end of the cylinder. We have laser-cut acrylic sheets and built a jig to limit the stroke of the pneumatic cylinder.

---

<sup>1</sup>Your average pneumatic cylinder would typically be made from metal and can be allowed to “bottom out”.

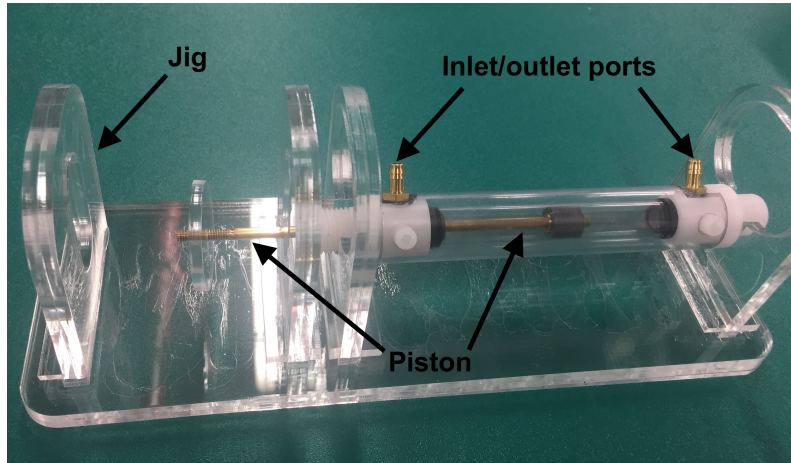


Figure 3.13: Double-acting cylinder

The two ports on the cylinder act as both inlets and outlets. Air is exhausted from the system through the the valves which have exhaust ports for when there is air flowing into one of its outlet ports.

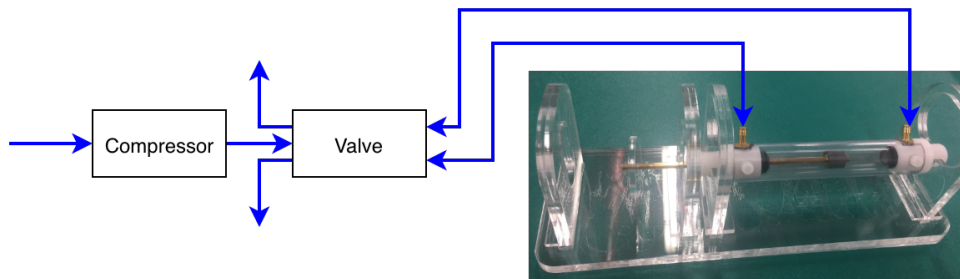


Figure 3.14: Pneumatic connections for the cylinder

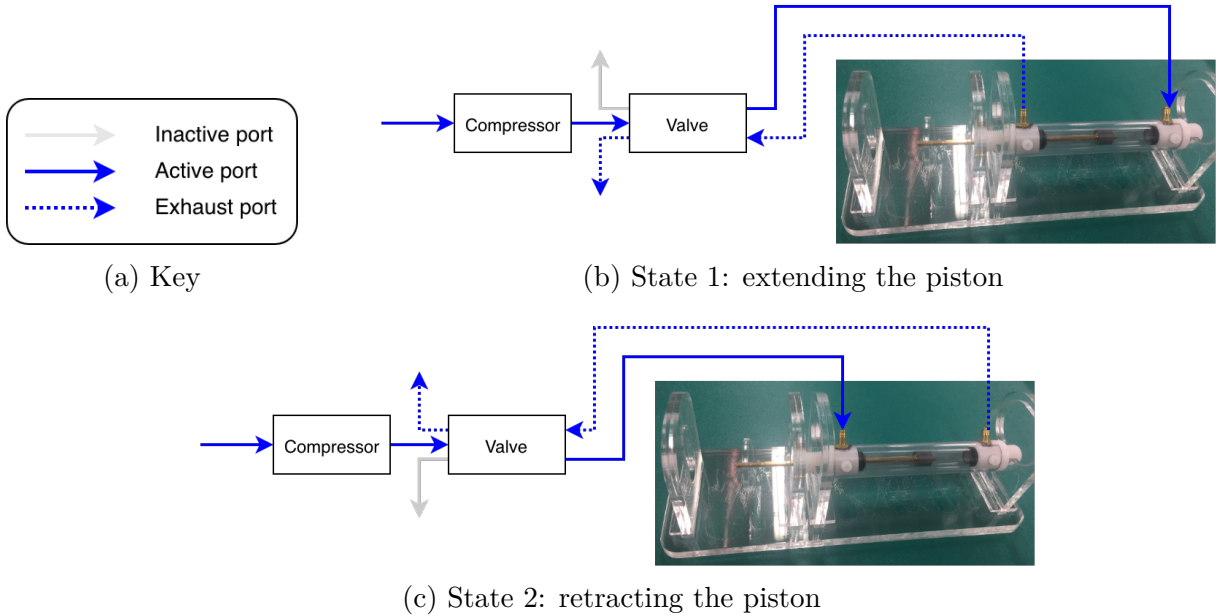


Figure 3.15: States in the pneumatic cylinder system

The electrical system for the pneumatic system has the exact same configuration as the Deprag air motor (Figure 3.12).

## 3.2 SNR Analysis

After building the actuators, we then examined the actuators' impact on image quality when placed inside an MRI scanner. To do this, we visited two MRI facilities and performed a series of tests to determine the SNR of a uniform phantom in the presence of each actuator during the scan. The scan images are stored as DICOM files, which were then processed on MATLAB. When performing SNR calculations on the scan images, the phantom is defined as our simulated signal of interest for consistency in measurement – what we are really interested in measuring is the effect of our test items on the phantom SNR.

In addition to testing the four actuators described in Section 3.1, we also tested an optical encoder and a linear slide. While the encoder and linear slide are not actuators them-

selves, we decided to test them as well because they are common components that could potentially be built into a robotic system.

Many of these components require peripheral equipment to power the device – e.g. controllers, drivers, valves, etc... – but most, if not all, of these devices are ferromagnetic and cannot be placed inside an MRI scanner. Instead, the peripheral equipment remain outside of the scan room, with only the essential wires and tubes being passed into the scan room via a waveguide.

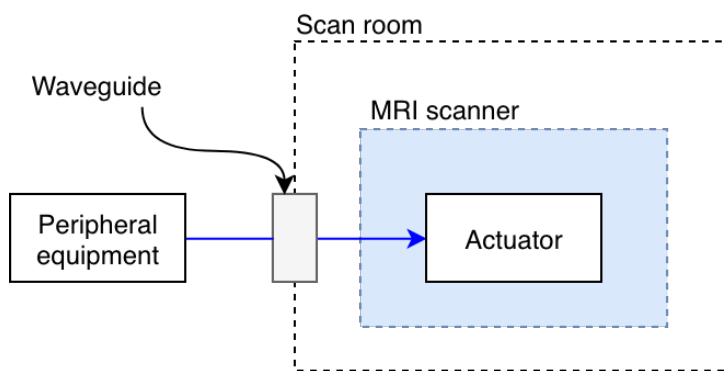


Figure 3.16: Equipment setup during test scans

Unfortunately, we could not test the ceramic motor system in closed loop because the jig was too big to fit into the 7T small animal system. Although the closed loop ceramic motor was ready to be tested on the 1.5 MRI-LINAC, not everything happened according to plan. This tragic story is recounted as a footnote<sup>2</sup>. Not being able to test the ceramic motor in closed loop means that we cannot quantify the SNR losses of the optical encoder and linear slide whilst moving, and can only test them while stationary.

---

<sup>2</sup>The Galil Motion Controller does not support my laptop's operating system, so I had been compiling and uploading code from a university desktop computer. With no viable way of uploading new code at the testing facility and only one controller to go around, our solution was to borrow a controller from a different project and upload the open loop code to one controller, and the closed loop code to the other controller. Breaking the hardware rule of not changing anything right before testing, one of our controllers did not work on the day, naturally.

### 3.2.1 Testing SNR on the 7T small animal system

The first facility we tested on was the MR Solutions 7T small animal system at the University of Sydney Charles Perkins Centre. This scanner was designed for small animals (usually rodents), and is thus relatively small in size (see Figure 3.18). The way we conducted this experiment was to position a falcon tube of water in the middle of the RF coil to act as the uniform phantom, and then placed our test item as close as possible to the phantom without touching it. The field of view (FOV) sliced through the middle of the phantom, as shown in Figure 3.17. The test items were positioned outside but adjacent to the FOV, which would still impact on the image SNR if there were any MR-incompatibility issues in the test item.

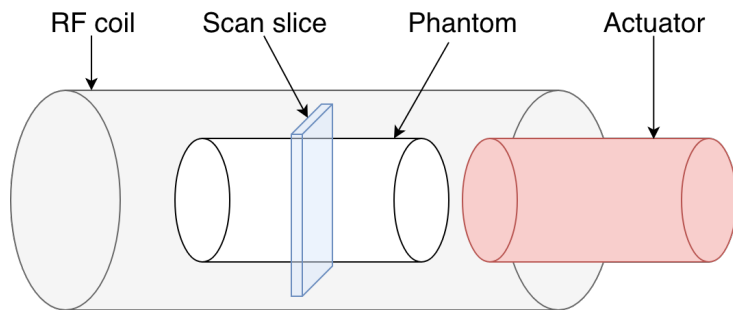


Figure 3.17: Phantom and scan slice setup

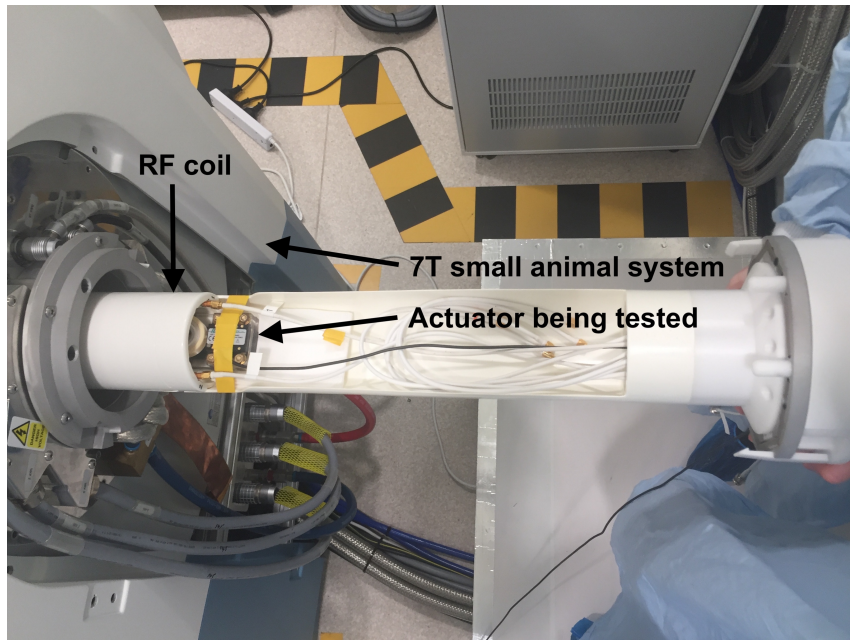


Figure 3.18: A ceramic motor is loaded at the edge of an RF coil, ready to be tested on the 7T scanner. Hidden from view is the falcon tube sitting in the middle of the RF coil.

Except for the rotary stepper motor, which was too large to fit inside the scanner, we were able to test the following equipment in the following configurations:

Item	Stationary	Moving
Air motor	✓	✓
Ceramic motor (open loop)	✓	✓
Cylinder	✓	✓
Optical encoder	✓	
Linear slide	✓	
Stepper motor		

Table 3.3: Test configurations on the 7T small animal system

While the air motor, cylinder, and stepper motor were scanned in the stationary configuration, the air compressor and valves were left switched on because in a realistic scenario, a actuator would still have its peripheral equipment powered on even during stationary

moments in its operation. Thus, if a motor was to demonstrate a decrease in SNR while moving compared to when it's stationary, the difference would be a result of the interaction between the actuator movement and the changing magnetic field gradient of an MRI scanner.

The same is true for the ceramic motor: the drivers and controllers were left switched on during the stationary tests because the robotic platform is intended to be switched on for the duration of the benchmarking process.

For each configuration, we were able to take three scan images using a spin echo (SE) sequence.

Scan parameter	Value
Sequence	SE
Repetition time	1000ms
Echo time	11ms
Slice thickness	3mm
Field of view	60mm x 60mm
Image resolution	128 x 256
Phantom type	water-filled falcon tube

Table 3.4: MRI scan parameters for our first test on the 7T small animal system

Once we obtained the scan images, we then processed the images on MATLAB to produce a value for SNR. SNR is calculated as thus:

$$SNR = \frac{\mu_{signal}}{\sigma_{noise}}, \quad (3.1)$$

where  $\mu_{signal}$  is the mean of the signal region of interest (ROI) and  $\sigma_{noise}$  is the standard deviation in a background ROI.

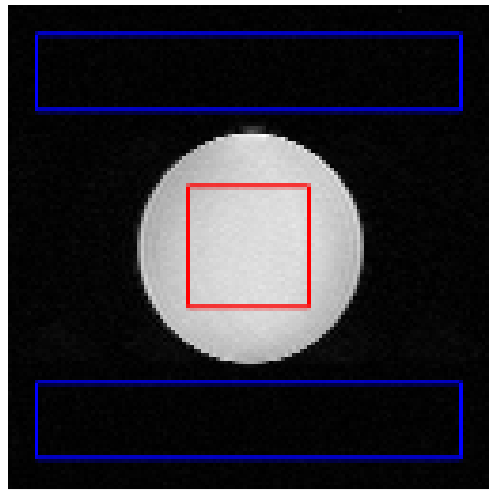


Figure 3.19: Red = signal ROI, blue = background noise ROIs

The signal ROI was taken at the centre of the phantom, whilst the background ROI was taken as two horizontal rectangular boxes above and below the phantom. The signal and background ROIs were chosen under the recommendations of the researchers assisting our experiments on the 7T small animal system.

### 3.2.2 Testing SNR on the 1.5T MRI-LINAC

The second facility we tested at was the 1.5T MRI-LINAC at the Ingham Institute in Liverpool, Sydney. We were able to test two different types of scan sequences on the 1.5T MRI-LINAC:

1. SE: similar to the tests on the 7T small animal system, this sequence produces a single scan image acquired over the duration of a certain number of seconds.
2. half-Fourier acquisition single-shot turbo spin-echo (HASTE): whereas the SE sequence produces a scan image, the HASTE sequence can be thought of as the video equivalent of MRI scan images. Acquiring multiple scans over a longer duration of time allows us to measure the change in SNR over time as we switch on/off different

actuators. For our experiment, we switched on the motors halfway through the HASTE scan duration.

<b>Scan parameter</b>	<b>Value</b>
Sequence	SE
Repetition time	1000ms
Echo time	30ms
Slice thickness	5mm
Field of view	300mm x 300mm
Image resolution	256 x 256
Phantom type	gadolinium-doped water-filled sphere

Table 3.5: MRI scan parameters for test one on the 1.5T MRI-LINAC

<b>Scan parameter</b>	<b>Value</b>
Sequence	HASTE
Repetition time	500ms
Echo time	98ms
Slice thickness	5mm
Field of view	300mm x 300mm
Image resolution	128 x 128
Number of frames	120
Phantom type	gadolinium-doped water-filled sphere

Table 3.6: MRI scan parameters for test two on the 1.5T MRI-LINAC

Similar to our experiments on the 7T small animal system, the phantom was the signal of interest, and was placed at the centre of the FOV. For this set of experiments, we used a gadolinium-doped water-filled sphere as the uniform phantom. Also, the RF coil is much larger in the MRI-LINAC because it is designed to fit human patients, so all the

components were able to fit very comfortably, including the rotary stepper motor, which did not fit inside the 7T small animal system.

Item	Stationary	Moving
Air motor	✓	✓
Ceramic motor (open loop)	✓	✓
Cylinder	✓	✓
Optical encoder	✓	
Linear slide	✓	
Stepper motor	✓	✓

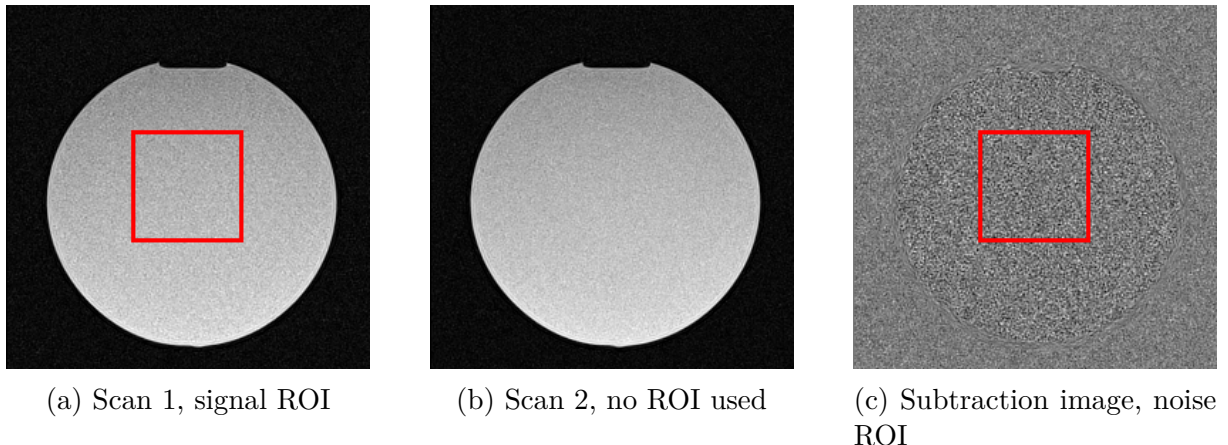
Table 3.7: Test configurations on the 1.5T MRI-LINAC

The SNR of each actuator was calculated using the dual acquisition, subtraction method described in Firbank et al [37]. This method uses two consecutive scans under the same conditions to acquire a single measurement for SNR, with the first scan acting as the signal image. Subtracting the second scan from the first scan then produces a subtraction image, which is taken to be the noise profile. The formula to determine SNR is defined as:

$$SNR = \sqrt{2} \frac{\mu_1}{\sigma_{1-2}}, \quad (3.2)$$

where  $\mu_1$  is the mean intensity in the signal ROI of the first scan and  $\sigma_{1-2}$  is the standard deviation in the noise ROI of the subtraction image [37].

Graphically, this is what the ROIs look like:



This method of calculating SNR is the standard procedure used by the researchers who work with the 1.5T MRI-LINAC. Note that this is different from the standard procedure recommended to us for the 7T small animal system experimental data.

### 3.3 Prototyping a pneumatic stepper motor

Having built and tested a ceramic motor and three pneumatic actuators, the next natural progression was to begin thinking about how a multi-axis robotic platform would look and what type of actuators can be scaled into the platform. From the results of our SNR analysis (see Section 4.2), it was deemed reasonable to rule out ceramic motors and pursue pneumatic actuators instead, the main reason being that ceramic motors consistently exhibited the worst SNR performance across all three sets of experiments.

For this next part of the project, there were two main sources of inspiration that guided the design of a pneumatic prototype actuator. The first is a pneumatic stepper motor design which Groenhuis et al use in their needle insertion robots. What's special about this type of motor is that it exploits the switching of valves to drive the motor in discrete steps, thereby minimising the complexities of pneumatic control that would arise from trying to drive a motor through continuous control of pressure.

In the case of continuous control of pressure, there is the problem of compressibility of air and the transport delay as compressed air flows through the pneumatic lines which make feedback control difficult. In a stepper motor, transport delay and air compressibility is still a problem, but can be mitigated by setting the pressure above a minimum operating level where the motor can be expected to behave consistently. Groenhuis et al. have also demonstrated a curvilinear stepper motor in their most recent needle insertion robot design (Figure 3.21b).

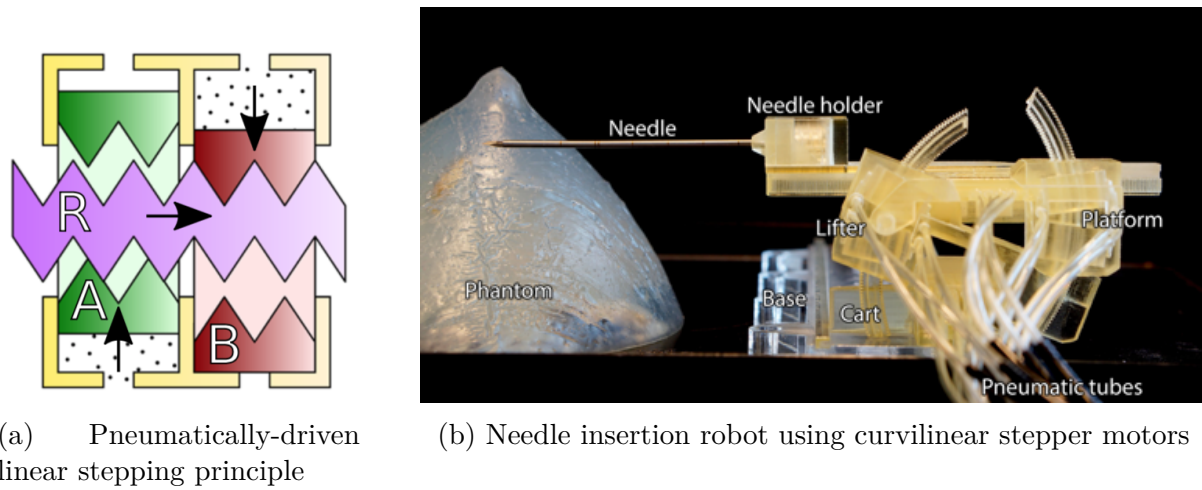


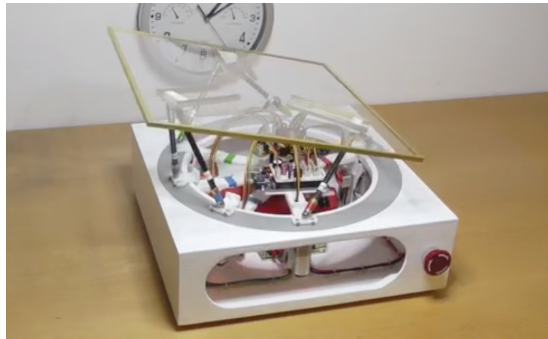
Figure 3.21: Stepper motors designed by Groenhuis et al (TODO: reference)

TODO: referencing!!!

The goal of this project is to work towards a robotic platform that can manipulate a phantom, which differs from a needle insertion robot in both its payload and the range of motion required. In the spirit of exploration and novelty, the latter half of this project involves combining the stepping principle demonstrated by Groenhuis et al with an unconventional Stewart platform design by an anonymous Youtube video, who named their design a circular base Stewart platform.

In a traditional Stewart platform, each of the six legs can independently extend and retract, which then causes the plate that rests on the six legs to change position and orientation. On the other hand, the circular base Stewart platform demonstrates a different

type of Stewart platform where the legs have fixed lengths but are able to slide around a circular track (Figure 3.23). This model was not designed for an MREnvironment, however, and would need some tweaking to make a pneumatic version of the circular base Stewart platform.



(a) A circular base Stewart platform. The legs have fixed lengths but are able to slide around a circular track.



(b) Underside view of Stewart platform – each leg is attached to a motor which drives the legs around the track.

### 3.3.1 Proof of concept

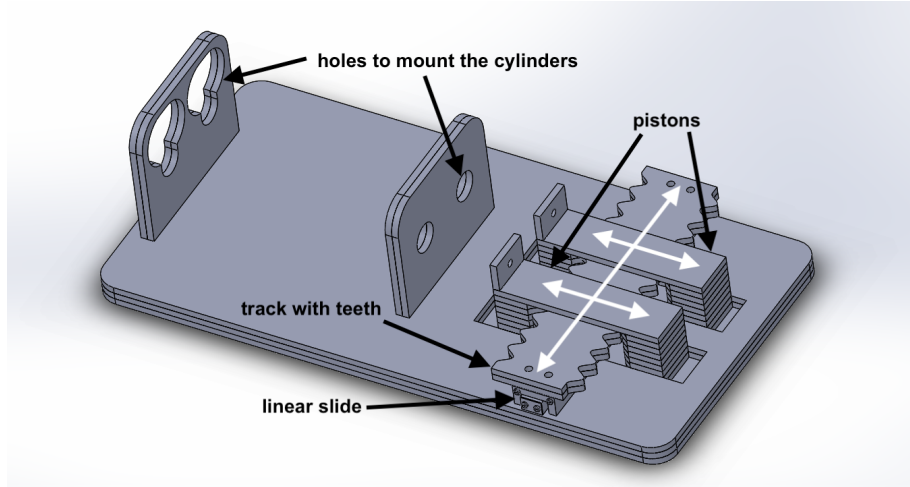


Figure 3.23: A jig to demonstrate the stepping mechanism

This model was made as a proof of concept to demonstrate the stepping mechanism that Groenhuis et al used in their designs. For our proof of concept, the idea was to use

existing parts we already had at hand and make a quick and dirty prototype. Instead of using four pressurised chambers, this proof of concept uses two pneumatic cylinders to drive the “pistons” (which are technically no longer pistons as there is also no longer a chamber that contains the “pistons”). A track with sinusoidal teeth was then mounted on the carriage of a linear slide to restrict the track to lateral movement.

### 3.3.2 Curvilinear stepper motor

Work then began prototyping a curvilinear stepper motor on Solidworks. Because the stepper motor must be mounted on a fixed circular track, there will have to be an opening in the motor housing to allow the track to protrude from the bottom and rest on a surface. This is different from Groenhui et al’s stepper motor which encloses the track completely.

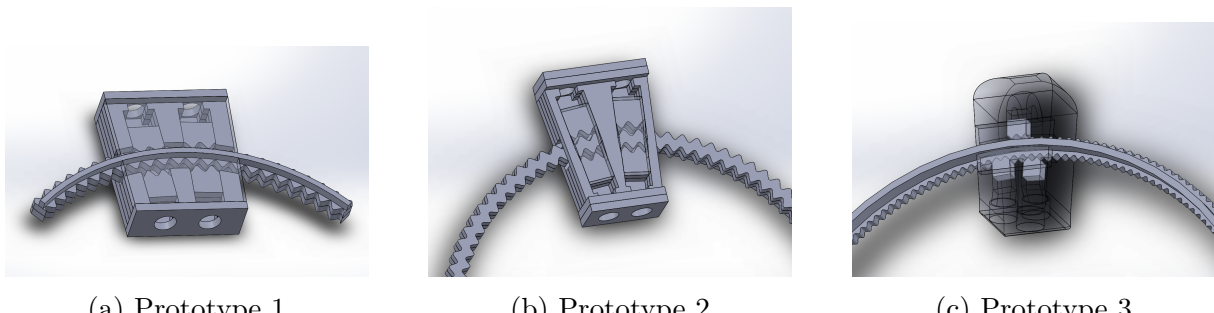


Figure 3.24: Three different iterations of design for a curvilinear stepper motor

The first two prototypes in Figure 3.24 have four chambers and pistons, which are connected so that the pistons move in pairs. Pressurising each chamber in a sequential pattern causes the motor to move around the circular track. If each time a new chamber is pressurised is called a ‘step’, then it takes four steps for the motor to traverse one cycle in the sinusoidal track.

The third prototype in Figure 3.24 is similar to the first two prototypes except that there are three individual chambers and pistons and it takes three steps to traverse one cycle in the sinusoidal track. Also, one of the chambers wraps around to the other side of the

motor so that the inlet ports are all on the same face on the motor for the sake of better tube management. The motor housing is slightly thicker for this prototype due to the wrapping of the inlet port.

### 3.3.3 Circular track

The stepper motor straddles a circular sinusoidal track, which is used to guide the motor as well as provide the teeth which the pistons can mesh with. The sinusoidal portion is enclosed by the motor housing, whilst the smooth circular portion is the part of the track that extrudes out from the motor.



Figure 3.25: Circular track with sinusoidal teeth

The track geometry is defined by two circular standing waves, which are subsequently defined by the parametric equations:

$$x = (R + a \cdot \sin(n\theta)) \cdot \cos(\theta) \quad (3.3)$$

$$y = (R + a \cdot \sin(n\theta)) \cdot \sin(\theta) \quad (3.4)$$

where  $R$  is the radius of the circle (mm),  $a$  is the amplitude of the standing waves (mm),  $n$  is the number of waves in a revolution, and  $\theta$  is the parameter. Increasing  $R$  increases the size of the track,  $a$  determines the depth of the teeth, and  $n$  determines the step angle subtended by each tooth in the circular track. Specifically for these prototypes, the variables take on the values:

<b>Variable</b>	<b>Inner curve</b>	<b>Outer curve</b>
$R$ (mm)	75	80
$a$ (mm)	1.25	1.25
$n$	90	90
$\theta$	0 to $2\pi$	0 to $2\pi$

Table 3.8: Values for the standing wave parameters in the sinusoidal circular track.

### 3.3.4 Fabrication

To turn the Solidworks prototypes into real-life models, we have two types of fabrication techniques that were readily available at the AMME Fabrication Laboratory and also made sense for this prototype.

#### Laser cut acrylic

One fabrication method we used was to laser cut sheets of acrylic into the appropriate shape and then superglue the layers together to form a 3D model. The pieces were then sanded down lightly where smooth surfaces are critical, e.g. the piston and chamber surfaces, or the surfaces where the track is in contact with the motor housing. Acrylic was chosen over medium-density fibreboard (the only other freely available material) because of the smoother surface finish of acrylic.

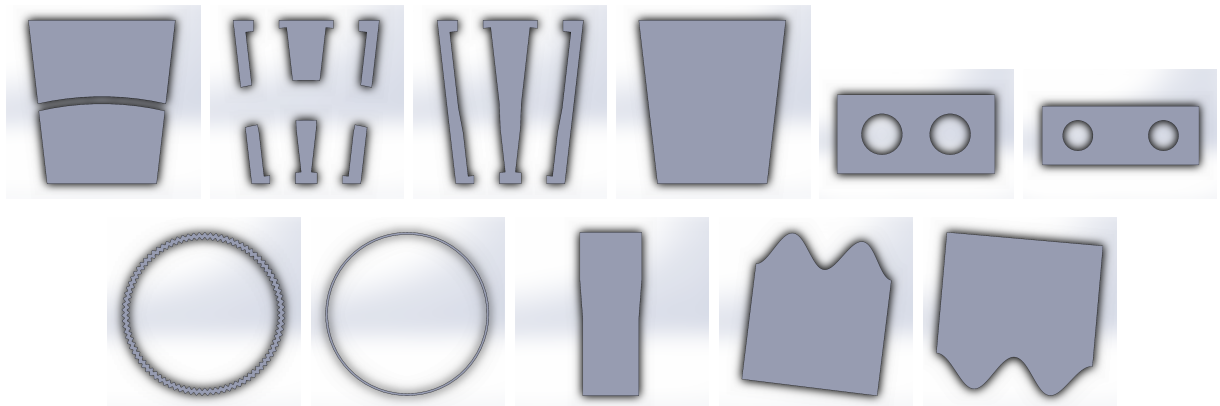


Figure 3.26: Example of all the distinct layers required for the prototype in Figure 3.24b (relative sizes are not to scale)

### Resin stereolithography

Another method of fabrication that we tested was stereolithography – i.e. 3D-printing resin. In stereolithography, a laser is aimed into a vat of resin, which semi-cures the resin into a solid layer-by-layer and can achieve micron-level layer thicknesses. The benefit of stereolithography is that it can generate very precise models which have a solid body, compared to fused deposition modelling (the more common 3D-printing method) of plastic filaments. A solid body is useful when attempting to create an airtight seal in the chambers of a pneumatic stepper motor. Stereolithography does not require the Solidworks prototype to be split into a number of layers and glue together – most of the parts can be fabricated in one piece.

After removing the semi-cured model from the printer, the model is immersed in isopropyl alcohol for 10 minutes to dissolve the excess uncured resin. At this point, the supports generated in the printing process can be snapped off. Then, the model is dried off and placed into a UV chamber for 10 to 30 minutes depending on the thickness of the parts. Finally, the final stage in the process is to sand down the surfaces, especially where the supports have not broken off cleanly.

### 3.3.5 Pneumatic control

For the four-chamber prototype in Figure 3.24, each piston must mesh fully with the track independent of the other three pistons, which means that only one chamber can be pressurised at a time. The following electrical and pneumatic connections were used to produce the stepping motion in our prototype actuator.

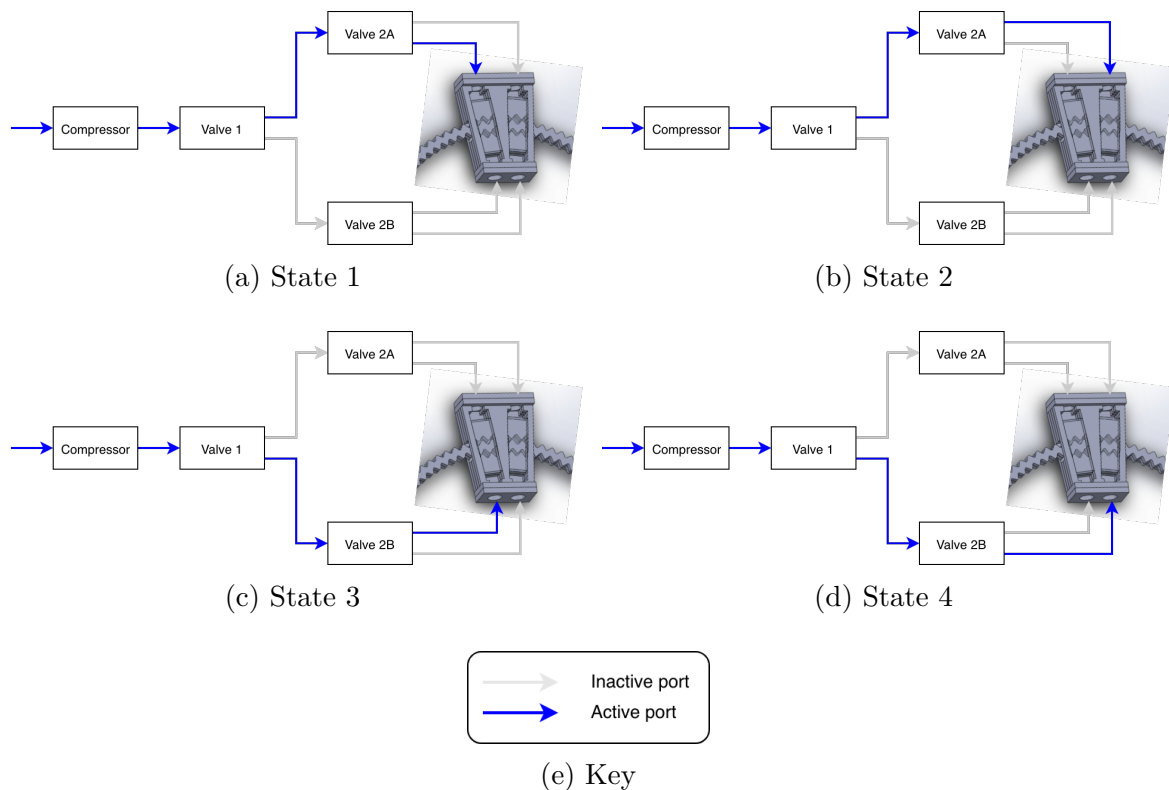


Figure 3.27: Compressed flow air through the pneumatic system in its four possible states. Switching the valves in the sequence state 1-2-3-4 produce a counterclockwise movement of the motor relative to the circular track. Switching in the sequence state 4-3-2-1 produces a clockwise movement of the motor relative to the track.

State	Valve 1	Valve 2A/B
1	Outlet 1	Outlet 1
2	Outlet 1	Outlet 2
3	Outlet 2	Outlet 1
4	Outlet 2	Outlet 2

Table 3.9: Activated outlet ports in each valve for each system state

Note that the valves labelled 2A and 2B share the same control signal in Figure 3.28, but are not pneumatically tethered together. Under this configuration, the control of the 4-chamber prototype is very simple: valve 1 switches at half the frequency of valves 2A/B.

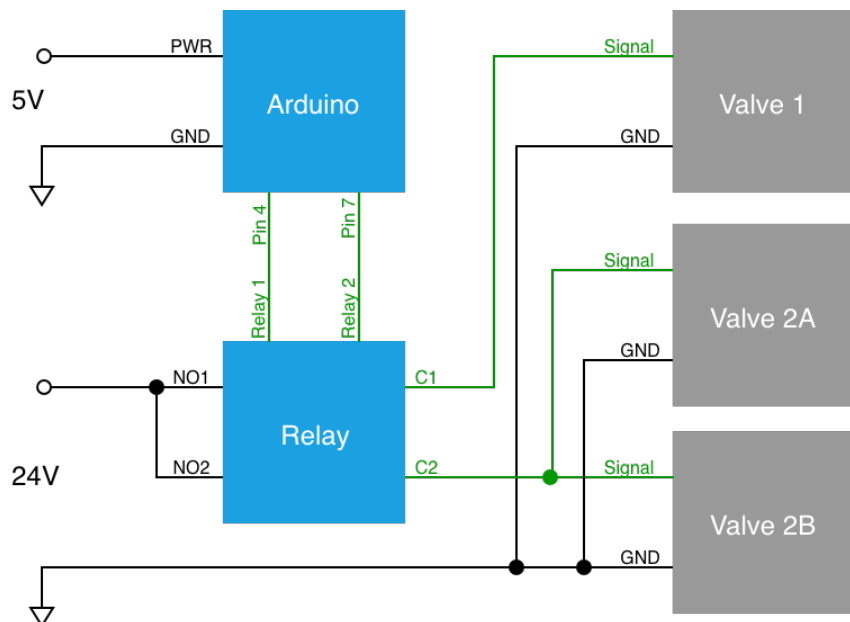


Figure 3.28: Electrical connections for the four-chamber prototype actuator

## 3.4 Actuator Characterisation

In the previous section, we have prototyped a series of curvilinear stepper motors. This section describes the next logical step in the process: to elect the best prototype and

characterise its performance in order to understand its scalability into a large robotic platform. It was through a few iterations of design-build-test, that the the second acrylic prototype emerged as the best motor to continue investigating. Thus, we devised a (very professional) pulley system with which we can test load and bandwidth performance of our prototype actuator, as shown in Figure 3.29.

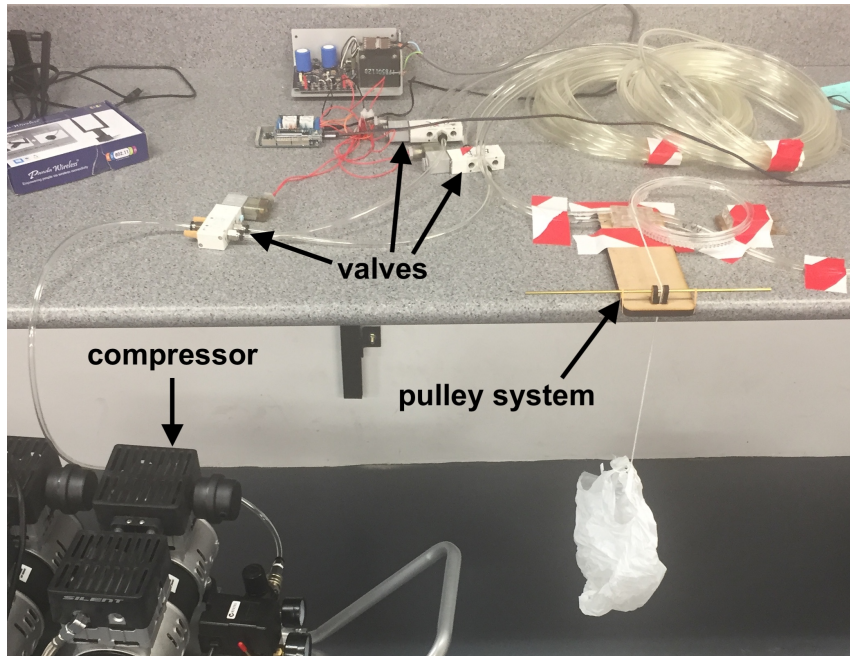


Figure 3.29: Bench-top setup for load and bandwidth tests. A bag is tethered to the end of the pulley system to hold the weights.

In this pulley system, the actuator is stationary while the track rotates to raise and lower the bag of weights. As the actuator raises the weights, it must also overcome the frictional forces of:

- The track in contact with the motor and the track support
- The pistons in contact with its chambers and the track teeth
- The string as it slides across the brass bar

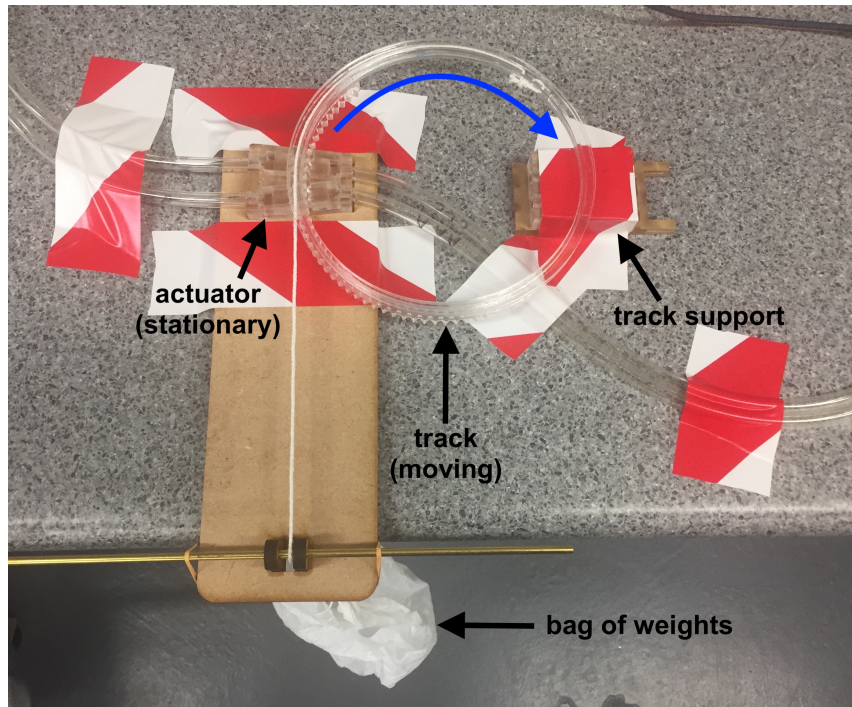


Figure 3.30: Close up of the pulley system

While the frictional forces in the system are unknown, we can however quantify the additional load of the weights acting tangentially to the circular track.

Item	Mass (g)
Bag	5
Weights (AAA batteries)	11
Track + string	42

Table 3.10: Known masses in the pulley system

### 3.4.1 Load tests

Load tests were conducted by driving the motor at a low step frequency and then adding weights to the pulley system until the motor stalled. The actuator was loaded with an initial mass of 47g from the track and the bag. What is being tested here was the additional load added to the system before the motor stalls.

First, the compressor gauge was fixed at 1 bar pressure. Then, the motor was operated through 10 cycles clockwise and then another 10 cycles counterclockwise. The reason the motor was clocked for 10 cycles in either direction is because the friction profile is not consistent for the whole arc length of the track, nor for each piston, so testing over a wider arc length would produce more consistent results between trials.

If at any point in the twenty cycles of operation the motor skipped a step or became stuck in one position, the motor was considered stalled. If the motor did not stall, a weight – we use AAA batteries as our weights – would be added to the pulley system and the twenty cycles would be repeated until the motor stalled. The total weight of all the batteries at stalling is considered the stall load. The whole experiment was then repeated for a variety of pressures from 1 bar to 3 bar in increments of 0.25 bar.

Here, a cycle is defined as: 1 cycle = 4 steps = 1 tooth arc travelled. Stall load is given by the equation:

$$L = \left( \frac{2n - 1}{2} \right) m_b g, \quad (3.5)$$

where  $L$  is the stall load (N), and  $n$  is the number of batteries at which the motor stall,  $m_b$  is the mass of the battery weights (kg), and  $g$  is gravitational acceleration at the Earth's surface ( $9.806\,65\text{ m s}^{-2}$ ). The factor  $2n - 1$  arises from the fact that the actual motor stalling occurs between  $n - 1$  and  $n$  batteries.

Parameter	Value
Stepping frequency	1 Hz
Pressures tested	1 bar - 3 bar
Pressure increments	0.25 bar
Initial mass	47g
Mass of weight increments	11g
Cycles per test	10 clockwise; 10 counterclockwise

Table 3.11: Experimental parameters for the load tests

### 3.4.2 Bandwidth tests

A bandwidth test was devised to determine the stepping frequencies the prototype actuator is able to achieve, which also gives an indication of the speeds the actuator is capable of. To maintain consistency with the load tests, the actuator was initially loaded with the weight of the track and the bag, although no additional battery weights were necessary for the bandwidth tests.

Bandwidth was tested for a range of pressures by decreasing the duration between steps until the motor stalls. The definition for motor stalling the same as for the load tests – i.e. when the motor misses a step or becomes stuck during a 20 cycle run. Whenever the actuator is able to complete a 20 cycle run successfully, the step duration is decreased by 2ms. Once the actuator reached a stall frequency, the whole experiment is repeated for a different pressure level.

Bandwidth was then calculated as:

$$f = \frac{1}{2} \left( \frac{1}{t} + \frac{1}{t - 0.002} \right), \quad (3.6)$$

where  $f$  is the maximum stepping frequency of the actuator (Hz), and  $t$  is the stepping

duration at which the motor stalls (s).  $f$  is thus the average of the upper and lower bounds for frequency due to the increment size of 2ms during the experiment.

Parameter	Value
Pressures tested	1 bar - 3 bar
Pressure increments	0.25 bar
Initial mass	47g
Step duration decrements	2ms
Cycles per test	10 clockwise; 10 counterclockwise

Table 3.12: Experimental parameters for the bandwidth tests

# Chapter 4

## Results

### 4.1 Preliminary actuator design

In this section, we will catalogue some of the performance properties observed in the preliminary actuators.

#### 4.1.1 Ceramic motor

The ceramic motor was successfully actuated to drive the ceramic bearing at approximately 1.5 revolutions/second in the open loop setting. In the closed loop setting, we were able to achieve point-to-point position control of the linear slide carriage, which was driven back and forth along its track once every two seconds.

#### 4.1.2 Pneumatic actuators

##### Rotary stepper motor

The rotary stepper motor was able to rotate its shaft in  $90^\circ$  increments with a nominal working pressure of 2 bar. The motor was also capable of reaching 10 Hz stepping

frequency at this pressure.

### Air motor

The air motor has a minimum operating pressure level of about 1.5 bar<sup>1</sup>, above which the motor was able to rotate its shaft in both direction. Below this approximate minimum pressure level, the motor would either not start up at all or would stall during its operation.

### Cylinder

The pneumatic cylinder performed binarised, end-to-end movements of its piston. The cylinder also had a minimum operating pressure level of around 1.5 bar<sup>1</sup>.

## 4.2 SNR Analysis Results

### 4.2.1 7T small animal system

The SNR performance of the moving air motor, whilst mild in SNR reduction, demonstrates a greater standard deviation in its results (Figure 4.1) than in all other test items. One plausible explanation for the variability in the moving air motor results is that the vibrations from the air motor cause a ringing artefact, which is related to the movement of a scan subject. The vibrating movements of the air motor are unpredictable and irregular, resulting in a scan image that is inconsistent between scans. Although all the scan images exhibit a small amount of ringing echo, this artefact is exacerbated in the moving air motor tests. In Figure 4.3, the ringing artefacts are excessive, even when compared to other moving test items.

---

<sup>1</sup>Number obtained through experience.

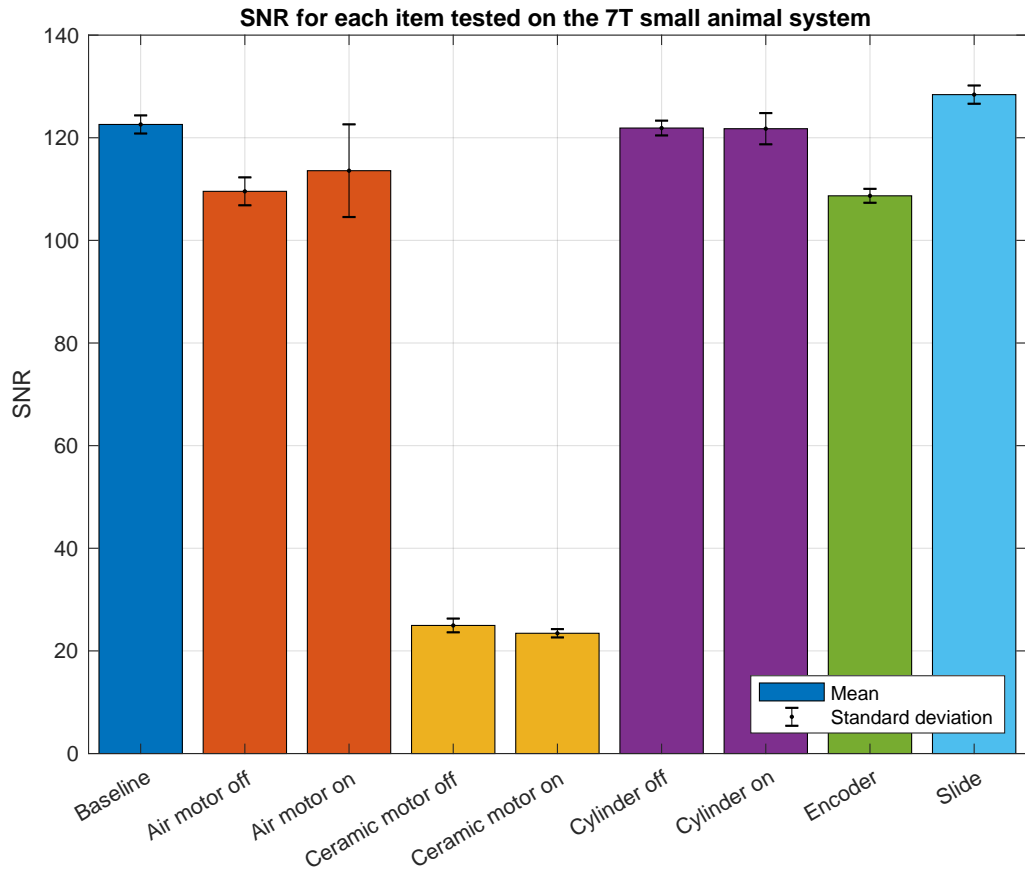


Figure 4.1: SNR results from the 7T small animal system

In the ceramic motor scan images for both stationary and moving configurations, there is a white line at the top of the image, which suggest RF interference. Small amounts of RF interference is observable in the other images in Figure 4.3, but is much more severe for the ceramic motor scans. Because the ceramic motor operates on a high-voltage low-current sinusoidal signal, the RF interference artefacts are likely to be a result of the interaction of the motor signal frequency and the MRI resonant frequency. The SNR results for the ceramic motor are consistently poor compared to the inconsistently decent results of the moving air motor due to the localisation of the RF interference artefact within a small region in the scan and consistency of the interference itself between scans.

On the 7T small animal system, SNR analysis demonstrates that:

- The pneumatic cylinder in both off and on configurations and the stationary linear slide exhibit minimal reductions in SNR
- The air motor in the off configuration and the stationary optical encoder exhibit mild, but still insignificant, reductions in SNR
- The ceramic motor in both off and on configurations exhibit a significant decrease in SNR

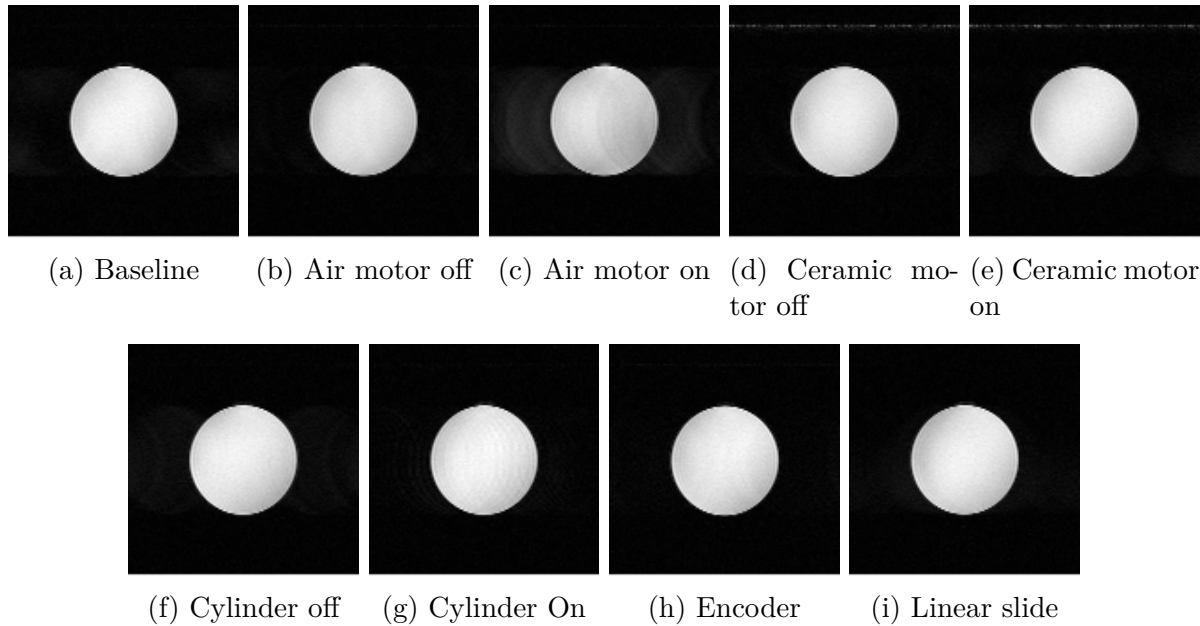


Figure 4.2: Sample original scan images from the 7T small animal system

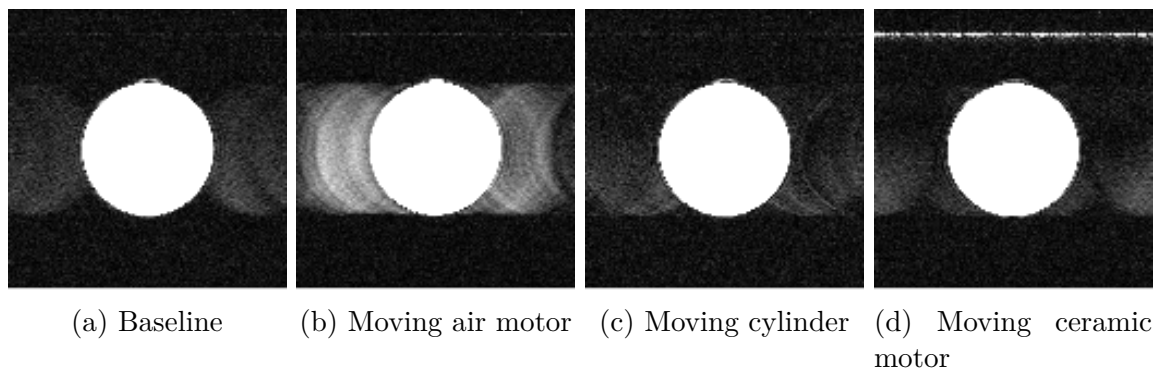


Figure 4.3: Sample scan images from the 7T small animal system with contrast adjusted to emphasise the image artefacts.

- The passive optical encoder and linear slide demonstrate good MR-compatibility.

### 4.2.2 1.5T MRI-LINAC

The SNR analysis results from the 1.5T MRI-LINAC experiments demonstrate similar findings to the 7T small animal system results. The pneumatic systems cause minimal degradation in SNR while the ceramic motors cause a moderate reduction when stationary and a drastic reduction when moving.

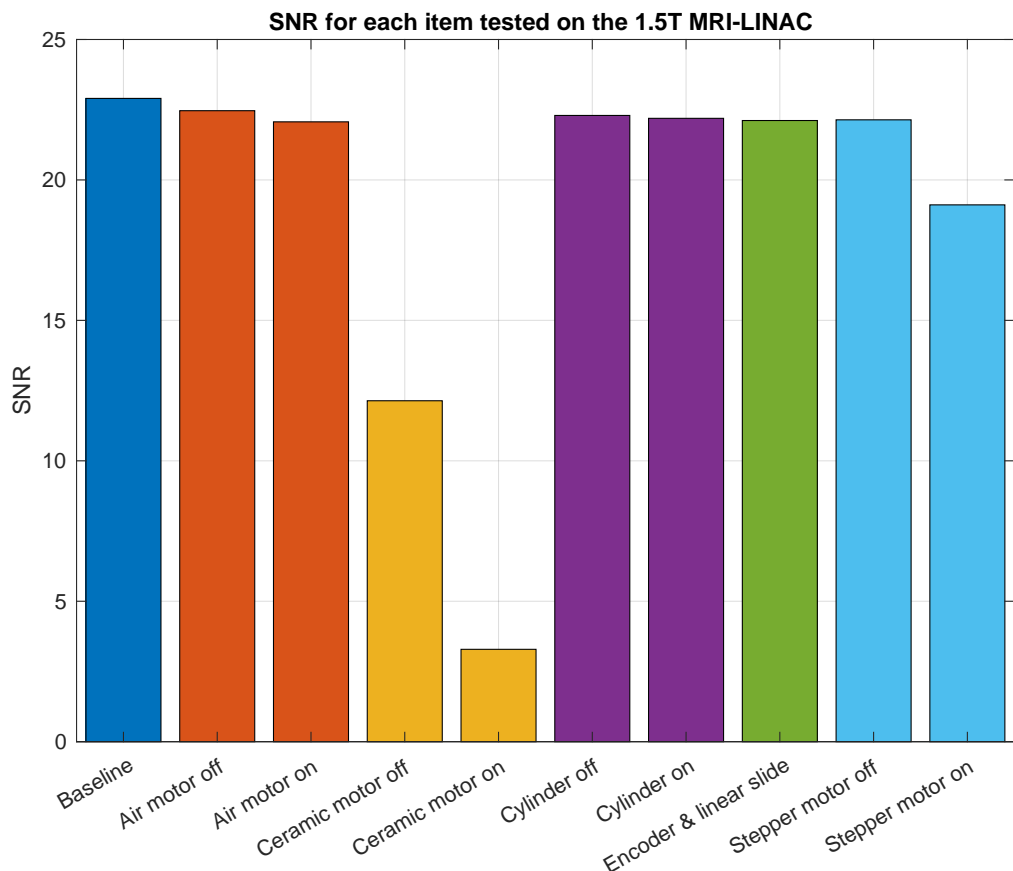


Figure 4.4: SNR results from the 1.5T MRI-LINAC (SE scans)

Unlike the 7T results, the air motor in a moving configuration did not exhibit a ringing effect from motion instability. Whereas in the 7T small animal system the air motor

is partially inserted into the RF coil and is in direct contact with the coil, in the 1.5T MRI-LINAC, the air motor was only in contact with the relatively stable bed and any transference of vibrations were negligible.

The scan images from the ceramic motor tests are more interesting. Without adjusting the contrast in the scan images, the RF interference artefacts when the ceramic motor is moving are immediately apparent in Figure 4.5e. Adjusting the contrast to emphasise the image artefacts (Figure 4.6), one can observe that there is random noise distributed

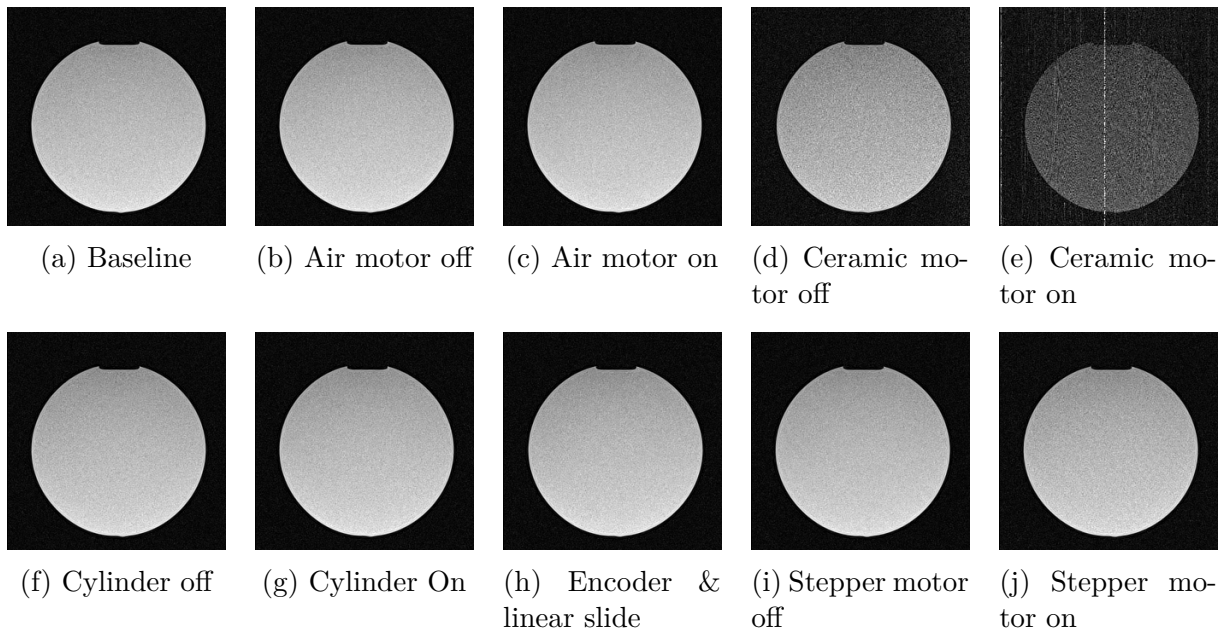


Figure 4.5: Sample scan images from the 1.5T MRI-LINAC (SE scans)

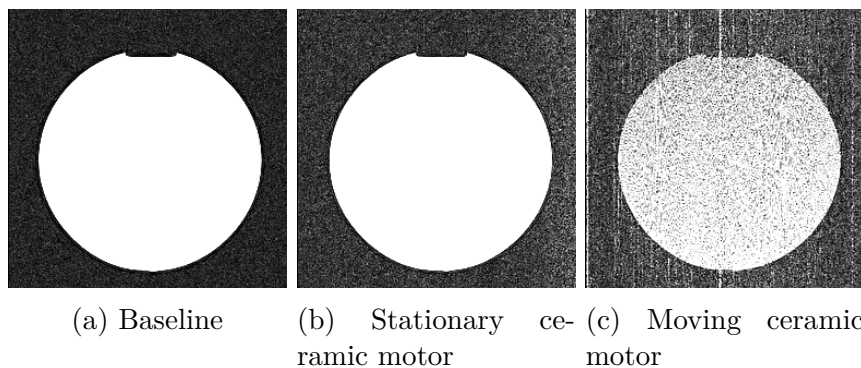


Figure 4.6: Sample scan images from the 1.5T MRI-LINAC with contrast adjusted to emphasise the image artefacts (SE scans)

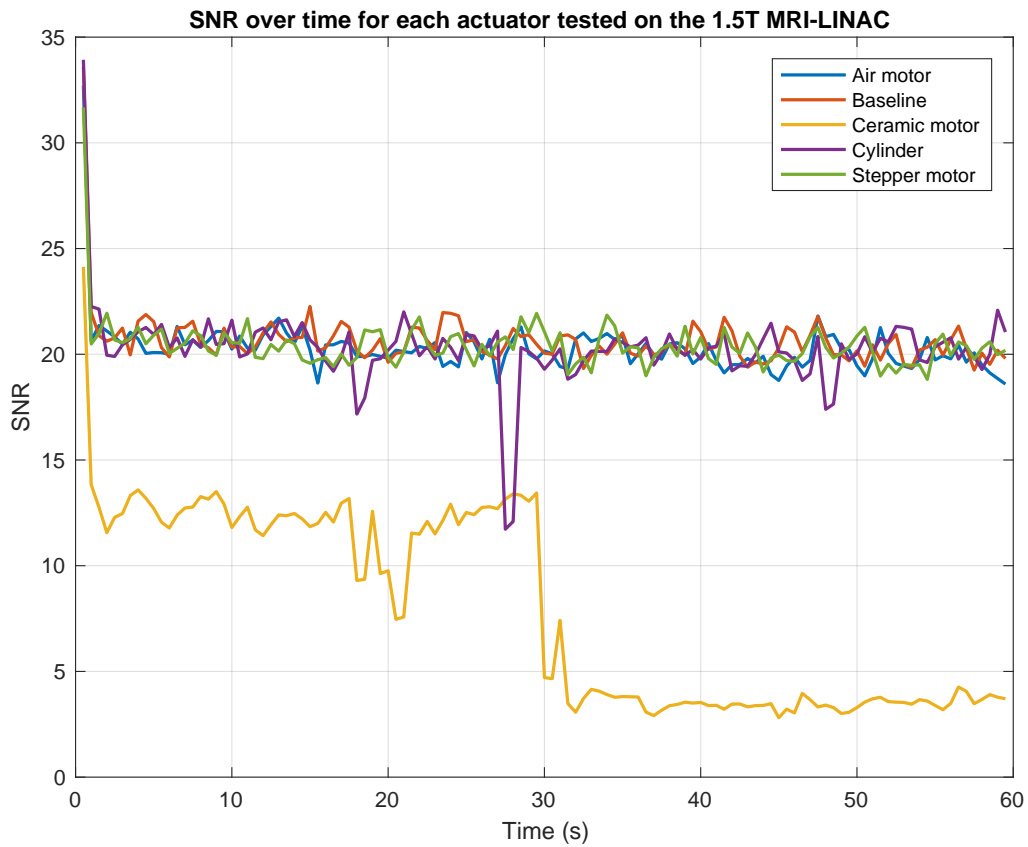


Figure 4.7: SNR results from the 1.5T MRI-LINAC (HASTE scans)

throughout the scan image when the ceramic motor is stationary, and that there are RF interference artefacts when the ceramic motor is moving.

Finally, results from the HASTE scan experiments also indicate that pneumatic system are more robust against SNR losses. For the ceramic motor, the drop in SNR is immediate even when stationary, and then drops even further once the motor begins moving.

## 4.3 Pneumatic motor prototyping

### 4.3.1 Proof of concept

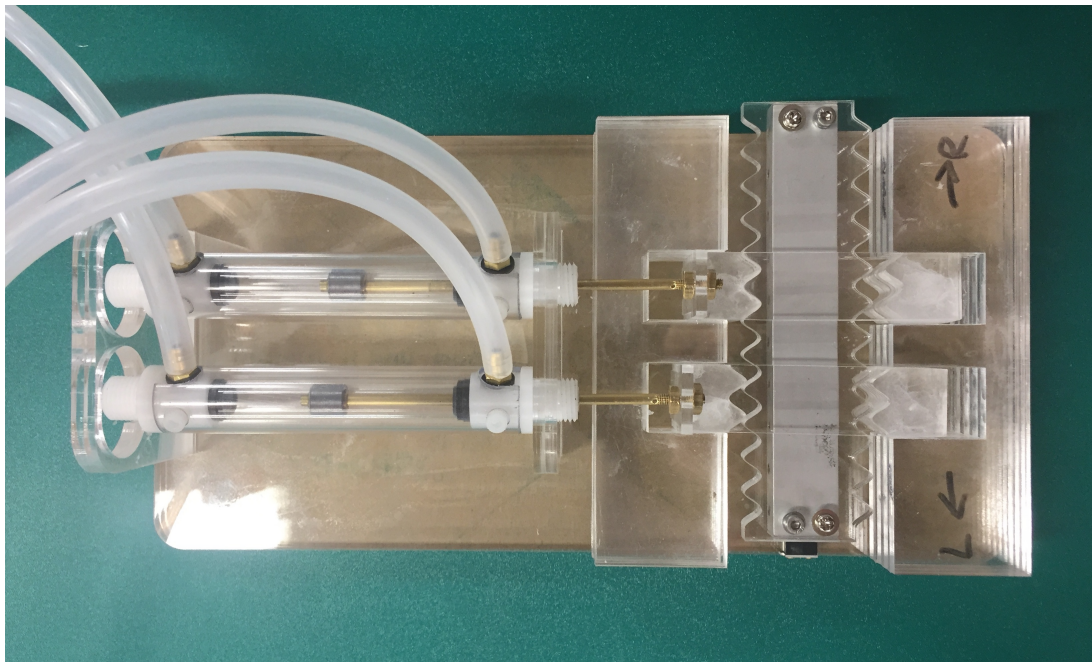


Figure 4.8: Proof of concept for stepping mechanism

The proof of concept model successfully demonstrated the stepping principle. The following list details some observational notes about the proof of concept model:

- Teeth depth: if the teeth are too deep, the track struggles to move because not enough force from the pistons is being translated into lateral movement in the track.
- Teeth shape: sinusoidally shaped teeth did not wedge as easily as triangular teeth. With sinusoidal teeth, there is less surface contact – and therefore, less friction – when the pistons engage and disengage with the track.
- Air pressure: the model requires a base pressure level in the cylinders before any of the pistons move. Below the minimum pressure requirement, the model cannot overcome the frictional forces required to move the pistons and the track.

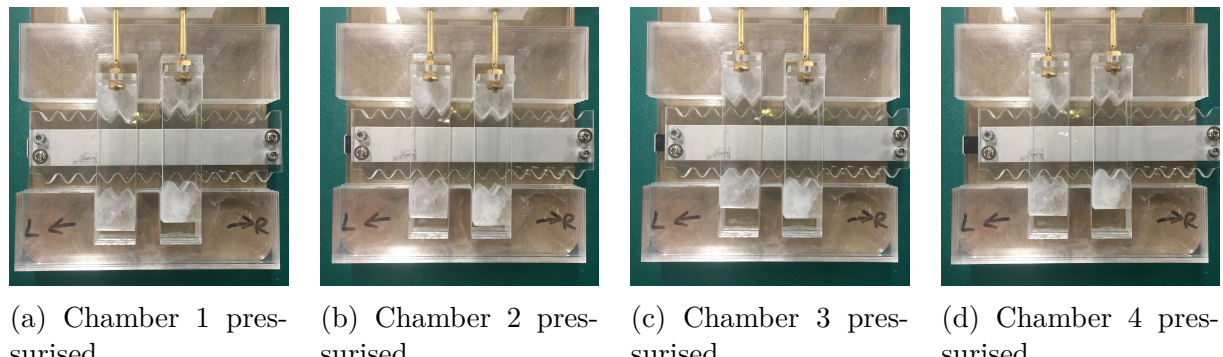


Figure 4.9: Pressurising chambers in the order 1-2-3-4 causes track to move to the right

### 4.3.2 Acrylic prototypes

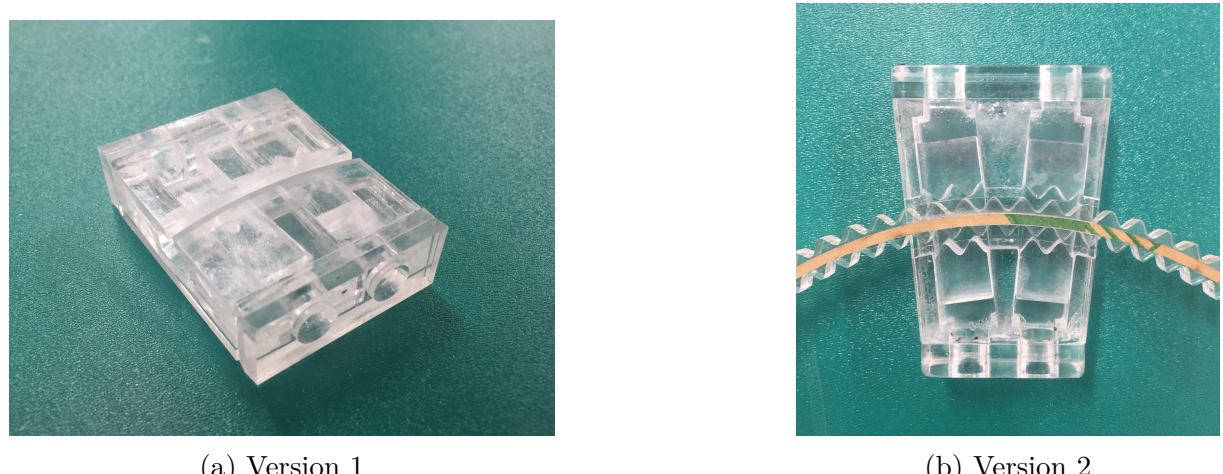


Figure 4.10: Acrylic prototypes – four chamber, curvilinear track design

Of the two acrylic prototypes that were fabricated, only version 2 was successful. The version 1 of this four chamber, curvilinear stepper motor design had misalignments due to the inaccurate angle and separation of the chambers. These geometric issues were resolved in the second version. Some things to note about the second acrylic prototype is that there was moderate air leakage out the sides of the motor and through cracks where the acrylic parts mate together.

### Resin prototypes



(a) Version 1 – four pistons



(b) Version 2 – three pistons

Figure 4.11: Resin prototypes – curvilinear track design

Both resin models proved to be unsuccessful prototypes. For both versions, there was shrinkage in the housing which prevented the pistons from meshing properly with the track. There was also a significant amount of friction from un-sanded surfaces in the resin model. In version 2 of the resin prototypes, the pistons proved to be too small for the tolerances that were built into the prototype. In other words, the gap between the piston and the chamber was too big relative to the size of the teeth, so that any rattling in the pistons would prevent the teeth from meshing with the track properly.

That said, choosing a different type of resin and refining the post-printing process can make the resin models a viable actuator, especially since these models have fewer mating edges where air tends to leak out of.

## 4.4 Actuator Characterisation

### 4.4.1 Load tests

The graph in Figure 4.12 shows that 1 bar pressure, the actuator did not move. From 1.25 bar to 3 bar, the actuator was able to achieve a stall load between 0.27N and 1.6N with a measurement error of 0.11N due to the increment size of the battery weights (11g).

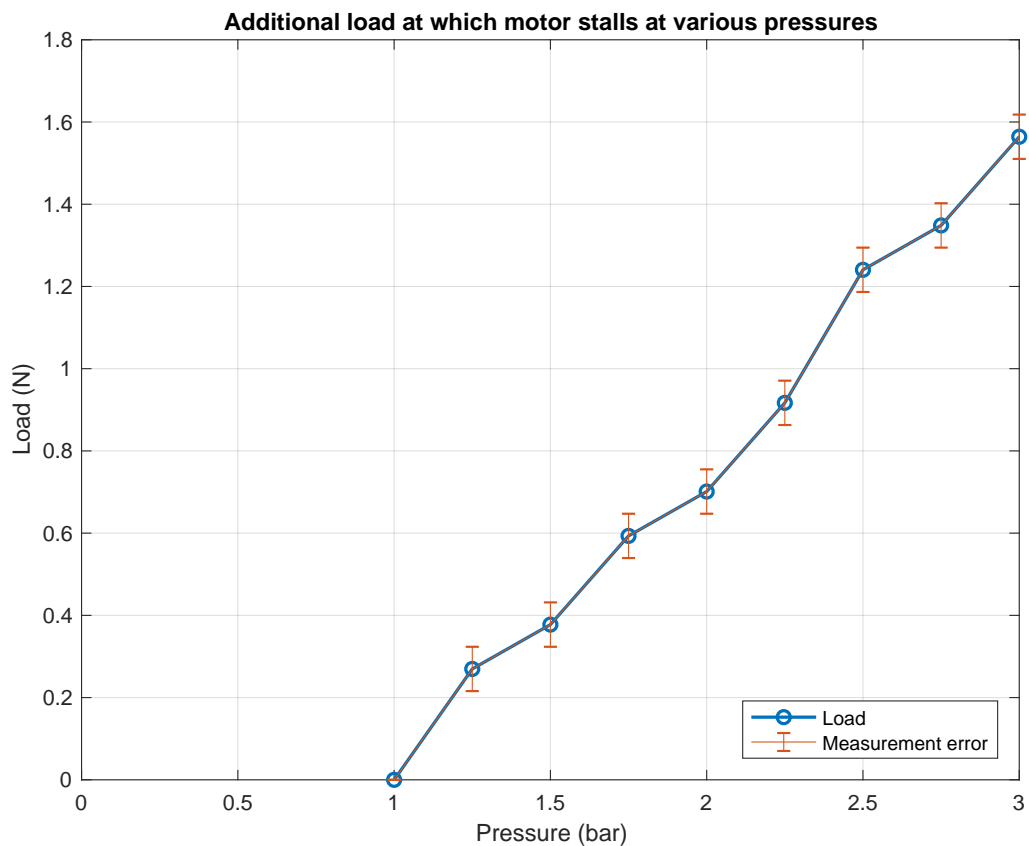


Figure 4.12: Experimental results for load capacity

### 4.4.2 Bandwidth tests

From the bandwidth tests, we are able to estimate the maximum stepping frequency of the actuator to be around 37 Hz, at which the measurement error is 1.4 Hz due to the

experimental increment size of the stepping duration (2ms). Experimental measurement error is at its minimum for long stepping durations (low frequencies) and at a maximum for short stepping durations (high frequencies), which is why the measurement error grows as the pressure increases and the resulting bandwidth increases.

Note, however, that the stepping frequency actually plateaus out to 37 Hz at around 2.25 bar pressure, which suggests that our pneumatic setup has an inherent bandwidth capacity that is not related to the power that the compressed air is able to deliver to the pistons.

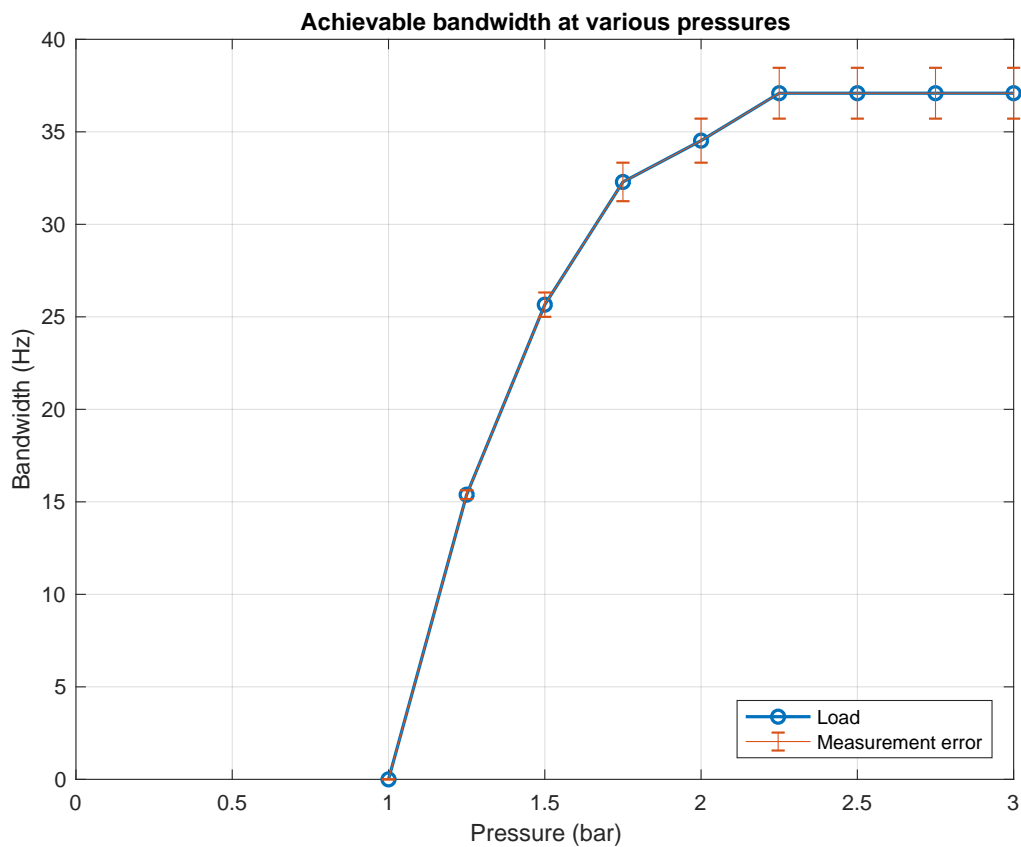


Figure 4.13: Experimental results for bandwidth capacity

# Chapter 5

## Discussion

The discussion chapter is split into four parts to mirror the sections in the methods and results chapters of this report.

### 5.1 Preliminary actuator design

In this section, we will discuss the performance of the preliminary actuators in a qualitative manner. While all four preliminary designs were able to produce actuation, some actuators have more practicality than others. Overall, we found that all four actuators showed potential but require further development to become .

#### 5.1.1 Ceramic motor

The ceramic motor was really compact in its open loop configuration, but quickly became bulky in its closed loop configuration. This is because the optical encoder itself is quite bulky and had to be coupled with an intermediate rubber wheel as the transmission (Figure 3.3), making this actuation less practical than it could be in the closed loop configuration. In future, it is absolutely possible to refine this design into a more practical and slimline model as others have achieved in the academic literature [3, 10].

### 5.1.2 Pneumatic actuators

#### Rotary stepper motor

The pneumatic rotary stepper motor, on the other hand, does not require feedback control as it can operate fairly predictably in an open loop configuration. The drawback for this type of motor is that its incremental steps are far too big  $90^\circ$  to be useful, thus requiring an additional gearbox to scale down the step sizes.

#### Air motor

Similar to the ceramic motor, the air motor is another compact design that requires careful consideration for closed loop control. The difficulties of developing a close loop system for continuous pneumatic control is explained in Section 2.3.2, and is relevant to the air motor which uses continuous control of pressure to adjust its speed.

#### Cylinder

The pneumatic cylinder was the bulkiest of the open loop actuators because of the jig required to limit the stroke of the piston. As an actuator, the cylinder performs quite reliably because of its minimal air leakage and low friction pistons. The cylinder would not be suitable as a single axis actuator in a robotic system because it can only perform binarised movements whereas for our purposes, the robotic system will need to follow a curve or trajectory. As an example of how pneumatic cylinders can be developed into a useful discrete actuator, Secoli et al. [18] have successfully prototyped a single-axis linear stepper motor that uses three cylinders in a binary fashion.

## 5.2 SNR Analysis

### 5.2.1 The poor MR-compatibility of ceramic motors

In all three SNR of the experiments that we performed across two MRI facilities, the ceramic motor showed the largest drops in SNR. This result is consistent with the SNR analysis results reported in the literature (see Section 2.3.1). Other researchers have investigated into this phenomenon but there is presently no general consensus on where the MR-incompatibility originates from or how best to mitigate its effects in an MRI scanner.

Aside from the effect of the low-current electrical signals that drive a ceramic motor, researchers have posited that the long wire of a ceramic motor acts as antenna to pick up external RF noise and transmit it into scan room [5–7, 38]. There is anecdotal evidence that techniques such as installing a filter panel in the scan room [31, 38] and putting the controller inside the scan room [5] can recover some SNR losses, but not all of it. There is also experimental evidence that RF shielding the ceramic motor cables minimises some of the SNR degradation [9].

While it’s true that these studies indicate potential for improving the MR-compatibility of ceramic motors, we decided to pursue pneumatic designs for the second half of this thesis project. The rationale for this decision was that pneumatics already have satisfactory MR-compatibility without the need for additional systems to recover any SNR losses.

### 5.2.2 Choice of ROI

In the 7T small animal system SNR analysis results, we found that the SNR performance of the air motor was similar to pneumatic cylinder, despite the presence of ringing artefact from the vibrations of the air motor (Figure 4.3). The fact that the air motor did not experience a significant drop in SNR is due to the choice of the background ROIs. The

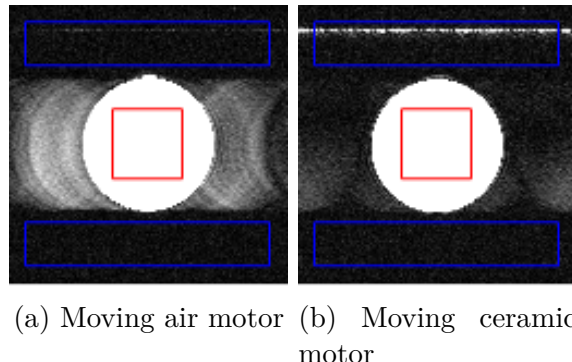


Figure 5.1: Contrast-adjusted scan image with ROI overlaid (7T small animal system) (red = signal ROI, blue = background ROI). Background ROI misses the ringing artefacts (left) but overlaps with the RF noise artefacts (right).

chosen background ROIs did not overlap with the ringing artefacts (Figure 5.1), even though the ringing artefacts do contribute to noise in the scan image. At the same time, the SNR losses from the ceramic motor were very significant because the RF noise artefacts landed inside the background ROIs.

We were recommended this choice of ROIs precisely to avoid the ringing artefacts because they are present to in all the experimental data from the 7T small animal system. The ringing artefacts are almost imperceptible in all scans except for the moving air motor.

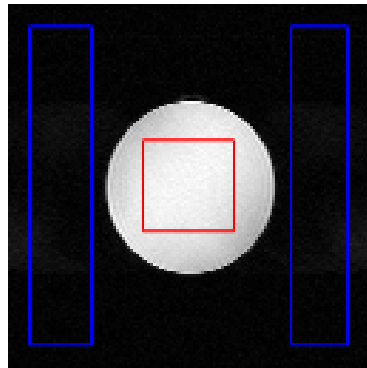


Figure 5.2: Vertical background ROIs for 7T small animal system data

If vertical background ROIs were chosen instead (Figure 5.2), the results would look significantly different as shown in Figure 5.3. The most obvious difference is that there is now a huge variability in SNR results for most of the test items, each of which was scanned

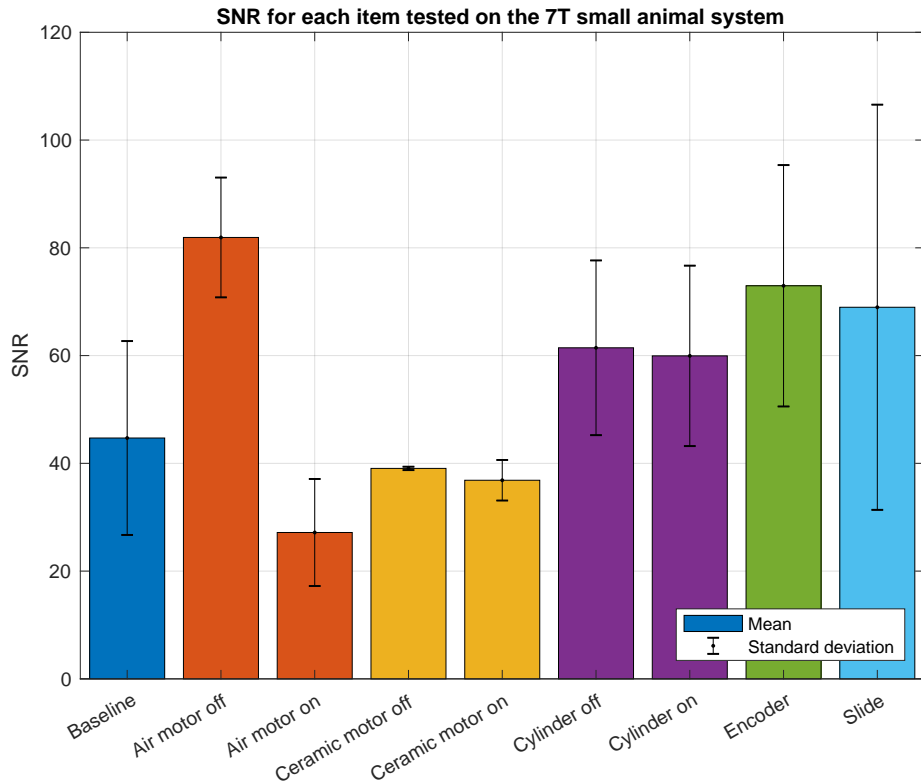


Figure 5.3: Hypothetical SNR analysis results for vertical background ROIs for the 7T small animal system data

three times. This extreme standard deviation range suggests that the ringing artefacts differ widely between scans of the same item. Unsurprisingly, the moving air motor demonstrated the lowest mean SNR. Even though this new choice of ROIs now takes into account the mild ringing artefacts of the air motor, the results are now meaningless because the differences in SNRs are statistically insignificant.

The point here is not to over-emphasise the significance of the motion artefacts. What this discussion attempts to do is to understand the unusually good results for the moving air motor given the motion artefacts present in its scan images.

## 5.3 Prototyping

### 5.3.1 Air leakage

Air leakage in the acrylic curvilinear stepper motor was an unavoidable problem because compressed air had to escape somewhere and we had not designed an exhaust path for the air to travel. Most exhaust air travelled out the sides of the motor where there was the largest opening.

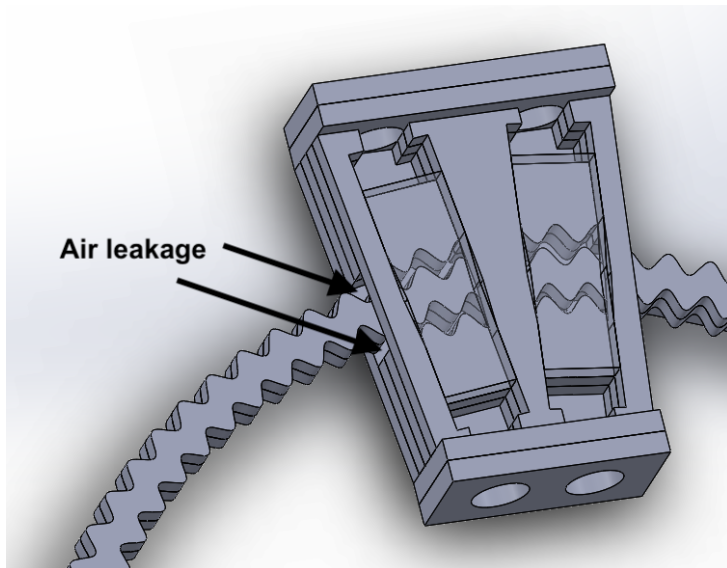


Figure 5.4: Most air leakage occurred at the sides of the acrylic curvilinear stepper motor

The problematic sources of air leakage were the cracks and crevices where the superglue did not create an airtight seal between acrylic layers. Some of these cracks were close to where the pneumatic hose delivers air to the chambers, thus reducing the efficiency of the compressed air acting on the pistons. One way we tried to mitigate this was by using Vaseline to form a seal in the chamber, but the oil was found to be too viscous and impeded the pistons' ability to move easily. Air tool oil was also used to lubricate the pistons and form a better seal in the chambers. The air tool oil ended up spraying everywhere because the fluid was so thin.

Air leakage was still present in the resin prototype, but it was less than in the acrylic prototype as the resin prototypes have a mostly resin solid body and fewer joined parts.

### 5.3.2 Friction and tolerancing

As the curvilinear stepper motor stepped around the circular track, we noticed that the motor would be slightly jerky at certain parts of the track because of friction that prevented the teeth from meshing fully. If the pressure was set low enough, the motor would even stall at those parts of the track. The take-home message here is that the curvilinear stepper motor system is like a chain – it will stall at the weakest tooth. This is why for the characterisation tests we actuated the stepper motor over a wide portion of the track in both directions: so as to get a fairer measurement of the overall performance of the motor in all stages around the track.

Consequently, proper tolerancing of parts is absolutely critical in this curvilinear stepper motor design because parts that are too tight would cause the motor to stall, and parts that are too loose would allow too much compressed air to escape, thereby making the motor less efficient.

## 5.4 Actuator Characterisation

### 5.4.1 Load tests

As shown in Figure 4.12, there appears to be a roughly linear relationship between air pressure and the maximum load the curvilinear stepper motor is able to drive before it stalls. One possible reason that this may be the case is that once the motor is able to overcome a base level of frictional forces, the motor is able to translate force from the compressed air to the pistons. Note also the equation for force due to pressure applied perpendicularly to a surface is given by the equation:

$$F = PA, \quad (5.1)$$

where  $F$  is the force (N),  $P$  is the air pressure (N/m<sup>2</sup>), and  $A$  is the area over which the pressure acts.

In the curvilinear stepper motor, compressed air acts over the same piston cross-sectional area, thus the force that is generated can be assumed to be approximately linear with pressure.

### 5.4.2 Bandwidth tests

In Figure 4.13, the bandwidth of the stepper motor can be seen to increase at a decaying rate as pressure is increased. There could be a number of limiting factors that cause the plateauing stepping frequency:

- Tube length: the longer the pneumatic tubes, the harder it is to switch pressures at a higher frequency. This is because air is highly compressible and has a long transport delay as it travels through the tube, therefore causing a low-pass filtering effect on the switching pressure levels.
- Mechanical inefficiencies: there may be a limit to the speed at which the pistons are able to mesh and unmesh with the toothed track due to the friction profile of the sliding surfaces.



# Chapter 6

## Conclusions

### 6.1 Summary

### 6.2 Future work

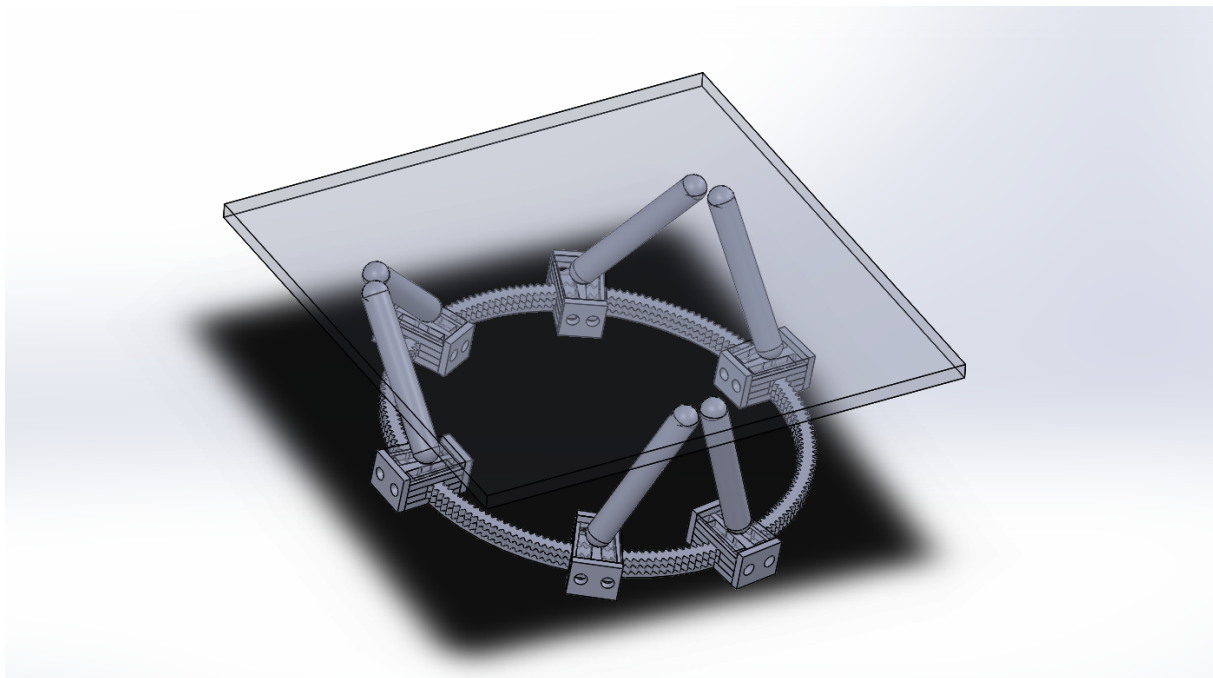


Figure 6.1: 6-DOF Stewart platform with curvilinear stepper motors as carriages on a circular track

# Bibliography

- [1] P. J. Keall, M. Barton, S. Crozier *et al.*, “The australian magnetic resonance imaging–linac program,” in *Seminars in radiation oncology*, vol. 24, no. 3. Elsevier, 2014, pp. 203–206.
- [2] N. Maughan, D. Muccigrosso, H. Schultejans, R. Bera, and P. Parikh, “Continuous tracking of lung tumor motion at 3.3 hz or faster is necessary to accurately represent motion,” *International Journal of Radiation Oncology? Biology? Physics*, vol. 96, no. 2, p. E679, 2016.
- [3] N. V. Tsekos, A. Khanicheh, E. Christoforou, and C. Mavroidis, “Magnetic Resonance-Compatible Robotic and Mechatronics Systems for Image-Guided Interventions and Rehabilitation: A Review Study,” *Annual Review of Biomedical Engineering*, 2007.
- [4] A. Berger, “How does it work?: Magnetic resonance imaging,” *BMJ: British Medical Journal*, vol. 324, no. 7328, p. 35, 2002.
- [5] R. Gassert, A. Yamamoto, D. Chapuis, L. Dovat, H. Bleuler, and E. Burdet, “Actuation methods for applications in MR environments,” *Concepts in Magnetic Resonance Part B: Magnetic Resonance Engineering*, 2006.
- [6] K. Chinzei, R. Kikinis, and F. A. Jolesz, “MR Compatibility of Mechatronic Devices: Design Criteria,” 1999.
- [7] G. S. Fischer, A. Krieger, I. Iordachita, C. Csoma, L. L. Whitcomb, and G. Fichtinger, “MRI compatibility of robot actuation techniques - A comparative study,” in *Lecture Notes in Computer Science (including subseries Lecture Notes in Artificial Intelligence and Lecture Notes in Bioinformatics)*, 2008.
- [8] N. V. Tsekos, A. Özcan, and E. Christoforou, “A prototype manipulator for magnetic resonance-guided interventions inside standard cylindrical magnetic resonance imaging scanners,” *Journal of biomechanical engineering*, vol. 127, no. 6, pp. 972–980, 2005.
- [9] A. Krieger, I. Iordachita, S.-E. Song, N. B. Cho, P. Guion, G. Fichtinger, and L. L. Whitcomb, “Development and preliminary evaluation of an actuated

- mri-compatible robotic device for mri-guided prostate intervention,” in *Robotics and Automation (ICRA), 2010 IEEE International Conference on*. IEEE, 2010, pp. 1066–1073.
- [10] H. Su, M. Zervas, G. A. Cole, C. Furlong, and G. S. Fischer, “Real-time mri-guided needle placement robot with integrated fiber optic force sensing,” in *Robotics and Automation (ICRA), 2011 IEEE International Conference on*. IEEE, 2011, pp. 1583–1588.
- [11] G. R. Sutherland, I. Latour, A. D. Greer, T. Fielding, G. Feil, and P. Newhook, “An image-guided magnetic resonance-compatible surgical robot,” *Neurosurgery*, vol. 62, no. 2, pp. 286–293, 2008.
- [12] K. Chinzei, N. Hata, F. A. Jolesz, and R. Kikinis, “Mr compatible surgical assist robot: System integration and preliminary feasibility study,” in *International Conference on Medical Image Computing and Computer-Assisted Intervention*. Springer, 2000, pp. 921–930.
- [13] E. Hempel, H. Fischer, L. Gumb, T. Höhn, H. Krause, U. Voges, H. Breitwieser, B. Gutmann, J. Durke, M. Bock *et al.*, “An mri-compatible surgical robot for precise radiological interventions,” *Computer Aided Surgery*, vol. 8, no. 4, pp. 180–191, 2003.
- [14] K. Masamune, E. Kobayashi, Y. Masutani, M. Suzuki, T. Dohi, H. Iseki, and K. Takakura, “Development of an MRI-compatible needle insertion manipulator for stereotactic neurosurgery,” *Computer Aided Surgery*, 1995.
- [15] B. Yang, U. X. Tan, A. B. McMillan, R. Gullapalli, and J. P. Desai, “Design and control of a 1-DOF MRI-compatible pneumatically actuated robot with long transmission lines,” *IEEE/ASME Transactions on Mechatronics*, 2011.
- [16] D. Stoianovici, A. Patriciu, D. Petrisor, D. Mazilu, and L. Kavoussi, “A new type of motor: Pneumatic step motor,” *IEEE/ASME Transactions on Mechatronics*, 2007.
- [17] A. Wineland, Y. Chen, and Z. T. H. Tse, “Magnetic resonance imaging compatible pneumatic stepper motor with geneva drive,” *Journal of Medical Devices*, vol. 10, no. 2, p. 020950, 2016.
- [18] R. Secoli, M. Robinson, M. Brugnoli, and F. Rodriguez y Baena, “A low-cost, high-field-strength magnetic resonance imaging-compatible actuator,” *Proceedings of the Institution of Mechanical Engineers, Part H: Journal of Engineering in Medicine*, vol. 229, no. 3, pp. 215–224, 2015.
- [19] J. Adam Cunha, I. C. Hsu, J. Pouliot, M. Roach, K. Shinohara, J. Kurhanewicz, G. Reed, and D. Stoianovici, “Toward adaptive stereotactic robotic brachytherapy for prostate cancer: Demonstration of an adaptive workflow incorporating inverse

- planning and an MR stealth robot," *Minimally Invasive Therapy and Allied Technologies*, 2010.
- [20] Y. Chen, C. D. Mershon, and Z. T. H. Tse, "A 10-mm MR-conditional unidirectional pneumatic stepper motor," *IEEE/ASME Transactions on Mechatronics*, 2015.
  - [21] A. Patriciu, D. Petrisor, M. Muntener, D. Mazilu, M. Schär, and D. Stoianovici, "Automatic brachytherapy seed placement under MRI guidance," *IEEE Transactions on Biomedical Engineering*, 2007.
  - [22] Z. Guo, Z. Dong, K.-H. Lee, C. L. Cheung, H.-C. Fu, J. D. Ho, H. He, W.-S. Poon, D. T.-M. Chan, and K.-W. Kwok, "Compact design of a hydraulic driving robot for intra-operative mri-guided bilateral stereotactic neurosurgery," *IEEE Robotics and Automation Letters*, vol. 3, no. 3, pp. 2515–2522, 2018.
  - [23] B. T. Larson, "Design of an MRI-Compatible Robotic Stereotactic Device for Minimally Invasive Interventions in the Breast†," *Journal of Biomechanical Engineering*, 2004.
  - [24] B. Yang, S. Roys, U.-X. Tan, M. Philip, H. Richard, R. P. Gullapalli, and J. P. Desai, "Design, development, and evaluation of a master–slave surgical system for breast biopsy under continuous mri," *The International journal of robotics research*, vol. 33, no. 4, pp. 616–630, 2014.
  - [25] V. Groenhuis, F. J. Siepel, J. Veltman, and S. Stramigioli, "Design and characterization of Stormram 4: An MRI-compatible robotic system for breast biopsy," in *IEEE International Conference on Intelligent Robots and Systems*, 2017.
  - [26] A. Krieger, R. C. Susil, C. Ménard, J. A. Coleman, G. Fichtinger, E. Atalar, and L. L. Whitcomb, "Design of a novel MRI compatible manipulator for image guided prostate interventions," *IEEE Transactions on Biomedical Engineering*, 2005.
  - [27] G. S. Fischer, I. Iordachita, C. Csoma, J. Tokuda, S. P. DiMaio, C. M. Tempany, N. Hata, and G. Fichtinger, "MRI-compatible pneumatic robot for transperineal prostate needle placement," *IEEE/ASME Transactions on Mechatronics*, 2008.
  - [28] D. Stoianovici, D. Song, D. Petrisor, D. Ursu, D. Mazilu, M. Mutener, M. Schar, and A. Patriciu, "'MRI Stealth' robot for prostate interventions," *Minimally Invasive Therapy and Allied Technologies*, 2007.
  - [29] R. C. Susil, K. Camphausen, P. Choyke, E. R. McVeigh, G. S. Gustafson, H. Ning, R. W. Miller, E. Atalar, C. N. Coleman, and C. Ménard, "System for prostate brachytherapy and biopsy in a standard 1.5 T MRI scanner," *Magnetic Resonance in Medicine*, 2004.

- [30] S. P. DiMaio, S. Pieper, K. Chinzei, N. Hata, S. J. Haker, D. F. Kacher, G. Fichtinger, C. M. Tempany, and R. Kikinis, “Robot-assisted needle placement in open MRI: System architecture, integration and validation,” in *Computer Aided Surgery*, 2007.
- [31] G. R. Sutherland, I. Latour, and A. D. Greer, “Integrating an image-guided robot with intraoperative MRI,” in *IEEE Engineering in Medicine and Biology Magazine*, 2008.
- [32] N. V. Tsekos, E. Christoforou, and A. Özcan, “A general-purpose MR-compatible robotic system,” in *IEEE Engineering in Medicine and Biology Magazine*, 2008.
- [33] N. White, C. Roddey, A. Shankaranarayanan, E. Han, D. Rettmann, J. Santos, J. Kuperman, and A. Dale, “PROMO: Real-time prospective motion correction in MRI using image-based tracking,” *Magnetic Resonance in Medicine*, 2010.
- [34] M. A. King, J. Dey, K. Johnson, P. Dasari, J. M. Mukherjee, J. E. Mcnamara, P. H. Pretorius, A. Konik, S. Zheng, and S. Miro, “Use of MRI to Assess the Prediction of Heart Motion by Stereo-Tracking of Markers on the Body Surface.”
- [35] C. Forman, M. Aksoy, J. Hornegger, and R. Bammer, “Self-encoded marker for optical prospective head motion correction in MRI,” *Medical Image Analysis*, 2011.
- [36] R. Ciric, D. H. Wolf, J. D. Power, D. R. Roalf, G. L. Baum, K. Ruparel, R. T. Shinohara, M. A. Elliott, S. B. Eickhoff, C. Davatzikos, R. C. Gur, R. E. Gur, D. S. Bassett, and T. D. Satterthwaite, “Benchmarking of participant-level confound regression strategies for the control of motion artifact in studies of functional connectivity,” *NeuroImage*, 2017.
- [37] M. J. Firbank, A. Coulthard, R. M. Harrison, and E. D. Williams, “A comparison of two methods for measuring the signal to noise ratio on MR images,” *Physics in Medicine & Biology*, vol. 44, no. 12, pp. 261–264, 1999.
- [38] G. Cole, J. Pilitsis, and G. S. Fischer, “Design of a robotic system for mri-guided deep brain stimulation electrode placement,” in *Robotics and Automation, 2009. ICRA '09. IEEE International Conference on.* IEEE, 2009, pp. 4450–4456.